Geological Magazine

www.cambridge.org/geo

Original Article

Cite this article: Ali S and Alshammari AS (2021) Genesis of gabbroic intrusions in the Arabian Shield, Saudi Arabia: mineralogical, geochemical and tectonic fingerprints of the Neoproterozoic arc magmatism. *Geological Magazine* **158**: 1639–1656. https://doi.org/10.1017/S0016756821000182

Received: 14 July 2020
Revised: 15 February 2021
Accepted: 24 February 2021
First published online: 12 April 2021

Keywords:
gabbro; Neoproterozoic; post-collisional magmatism; Arabian Shield; Saudi Arabia

Author for correspondence: Shehata Ali, Email: shehata.ali@mu.edu.eg

Genesis of gabbroic intrusions in the Arabian Shield, Saudi Arabia: mineralogical, geochemical and tectonic fingerprints of the Neoproterozoic arc magmatism

Shehata Ali[1] and Abdullah S. Alshammari[2]

[1]Geology Department, Faculty of Science, Minia University, 61519 El-Minia, Egypt and [2]Faculty of Science, Hail University, 2440 Hail, Saudi Arabia

Abstract

The Arabian Shield of Saudi Arabia represents part of the Arabian–Nubian Shield and forms an exposure of juvenile continental crust on the eastern side of the Red Sea rift. Gabbroic intrusions in Saudi Arabia constitute a significant part of the mafic magmatism in the Neoproterozoic Arabian Shield. This study records the first detailed geological, mineralogical and geochemical data for gabbroic intrusions located in the Gabal Samra and Gabal Abd areas of the Hail region in the Arabian Shield of Saudi Arabia. Geological field relations and investigations, supported by mineralogical and geochemical data, indicate that the gabbroic intrusions are generally unmetamorphosed and undeformed, and argue for their post-collisional emplacement. Their mineralogical and geochemical features reveal crystallization from hydrous, mainly tholeiitic, mafic magmas with arc-like signatures, which were probably inherited from the previous subduction event in the Arabian–Nubian Shield. The gabbroic rocks exhibit sub-chondritic Nb/U, Nb/Ta and Zr/Hf ratios, revealing depletion of their mantle source. Moreover, the high ratios of $(Gd/Yb)_N$ and $(Dy/Yb)_N$ indicate that their parental mafic melts were derived from a garnet-peridotite source with a garnet signature in the mantle residue. This implication suggests that the melting region was at a depth exceeding ~70–80 km at the garnet stability field. They have geochemical characteristics similar to other post-collisional gabbros of the Arabian–Nubian Shield. Their origin could be explained by adiabatic decompression melting of depleted asthenosphere that interacted during ascent with metasomatized lithospheric mantle in an extensional regime, likely related to the activity of the Najd Fault System, at the end of the Pan-African Orogeny.

1. Introduction

The Pan-African Orogeny represents tectonic, magmatic and metamorphic events that occurred during Neoproterozoic to earliest Palaeozoic time (Kröner & Stern, 2004). The orogenic cycle reveals the opening and closing of large oceanic realms along with the accretion and collision of buoyant crustal blocks. Pan-African activities culminated in the creation of the late Neoproterozoic supercontinent Gondwana. The Arabian–Nubian Shield (ANS) is one of the largest tracts of juvenile crust on Earth formed during the Neoproterozoic period, via accretion of arcs that existed between major fragments of East and West Gondwana (Stern, 2002; Johnson & Woldehaimanot, 2003; Meert, 2003; Stoeser & Frost, 2006; Abu-Alam *et al.* 2013).

Mafic–ultramafic assemblages of the ANS encompass ophiolitic and non-ophiolitic complexes. The ophiolitic complexes represent ancient oceanic lithospheric fragments formed in orogenic belts along major suture zones (Dilek & Furnes, 2011; Kakar *et al.* 2014; Abdel-Karim *et al.* 2016, 2018; Sedki *et al.* 2019; Ali *et al.* 2020). The non-ophiolitic complexes occur either as layered or as Alaskan-type gabbroic intrusions with some ultramafic rocks (Abd El-Rahman *et al.* 2012; Abdel Halim *et al.* 2016; Abdallah *et al.* 2019). The Alaskan-type intrusions are concentrically zoned intrusions emplaced during post-tectonic processes and are uplifted fragments of the deep levels of island arcs (Helmy *et al.* 2015; Abdallah *et al.* 2019). The mafic–ultramafic intrusions of Wadi Kamal, Hail and Lakathah in the Arabian Shield are akin to Alaskan-type intrusions (Collenette & Grainger, 1994; Harbi, 2008). In contrast, the layered intrusions occur as undeformed, small elliptical bodies along major structures, mostly lacking ultramafic rocks (El-Mettwaly, 1992; Azer & El-Gharbawi, 2011). The layered gabbroic intrusions comprise tholeiitic, calc-alkaline and alkaline rocks suggesting coeval derivation from different sources (Be'eri-Shlevin *et al.* 2009).

Mafic plutonism in the ANS was generated in diverse tectonic regimes. Older gabbro occurs as an essential part of obducted ophiolites and as a member of subduction-related metagabbro-diorite complexes. Ophiolitic and island-arc metagabbros are regionally metamorphosed up to

CAMBRIDGE UNIVERSITY PRESS

lower-amphibolite facies (El Ramly, 1972; El Sharkawy & El Bayoumi, 1979; Takla *et al.* 1981; El Gaby *et al.* 1990). Younger gabbro is mostly fresh intrusive mafic rock formed in a post-collisional setting (Takla *et al.* 1981; El Gaby *et al.* 1990; Khalil *et al.* 2015; Surour *et al.* 2017).

Mafic magmatism that occurred during Neoproterozoic time in the Arabian Shield documents two separate pulses (i.e. Cryogenian and Ediacaran) represented by older metagabbros and younger fresh gabbros (e.g. Johnson *et al.* 2011, 2013). Older metagabbros formed during Cryogenian time (~850–780 Ma) are rarely stratified and are related to calc-alkaline arc magmatism (Surour *et al.* 2017). Conversely, younger fresh gabbros were formed during Ediacaran time (~620–590 Ma) in a post-collisional regime following the late stages of arc amalgamation in the Arabian Shield (Surour *et al.* 2017).

Generally, the gabbroic intrusions in the Arabian Shield are poorly studied, lacking comprehensive geological, petrological, mineralogical and geochemical data. Recently, as far as we know, only one international paper by Surour *et al.* (2017) focused on the mineral chemistry of some gabbros from the Asir region in the western Arabian Shield of Saudi Arabia.

The present study deals with fresh gabbroic rocks located in the Gabal Samra and Gabal Abd areas of the Hail region (Fig. 1), which represents the northeastern part of the Arabian Shield. In fact, except for very little geological information presented in an old local report by Kellogg & Stoeser (1985), there are no comprehensive studies of these gabbros. These rocks are poorly studied as most studies focused on the granitic intrusions (e.g. Robinson *et al.* 2015*a*,*b*; Abdallah *et al.* 2020). So, this study presents the first detailed geological, mineralogical and bulk-rock chemical data for these rocks. The new data were used to better understand the tectonic setting of the Neoproterozoic mafic magmatism in the Arabian Shield and to constrain the nature of the mantle source as well as the conditions of crystallization and melting.

2. Geological setting

The ANS was produced during Neoproterozoic time (900–550 Ma) by accretion of intra-oceanic arcs during the Mozambique Ocean closure and Gondwana amalgamation (Ali *et al.* 2015). The subduction process started at ~870 Ma followed by arc–arc convergence and terrane suturing at ~780 Ma (Johnson & Woldehaimanot, 2003). These events mark the beginning of ocean closure and Gondwana assembly. The terrane amalgamation proceeded until ~600 Ma, causing juxtaposition of East and West Gondwana. The final assembly of Gondwana was reached by ~550 Ma following overlapping phases of basin creation, rifting, compression, strike-slip faulting and gneissic dome formation in association with extension and/or thrusting (Johnson & Woldehaimanot, 2003).

The diverse tectonic features of the post-amalgamation events indicate that the final assembly of Gondwana required alternating episodes of late Neoproterozoic extension and shortening, uplift, and depression, deposition and erosion (Johnson & Woldehaimanot, 2003). The Najd Fault System comprises late Neoproterozoic NW- and NE-trending strike-slip faults and shear zones affecting the northern part of the Arabian Shield (Johnson & Woldehaimanot, 2003). The NW-trending faults are common and generally sinistral, whereas the NE-trending faults are subordinate and dextral. These strike-slip faults were formed at ~640–540 Ma (Abdelsalam & Stern, 1996). Both trends of the fault sets form a conjugate pair.

The Arabian Shield of Saudi Arabia, a part of the ANS, forms an exposure of juvenile continental crust on the eastern side of the Red Sea rift. The Hail region is situated on the northeastern part of the Arabian Shield (Fig. 1a). A small NW-trending fault with apparent sinistral offset was documented in the Hail region, possibly related to the Najd Fault System (Delfour, 1981). Granitic and gabbroic intrusions together with numerous dyke swarms were emplaced during the regional extension of the Arabian Shield (e.g. Surour *et al.* 2017; Abdallah *et al.* 2020). Late Proterozoic intrusive rocks occupy the southern section of the Hail region. The rest of the region is covered by the Cambrian–Ordovician Saq sandstone and Ordovician–Devonian Tabuk Formation. Two assemblages of Precambrian intrusive rocks were recognized in this region (Kellogg & Stoeser, 1985). An older, partially deformed, orogenic assemblage (>620 Ma) comprises rocks ranging from gabbro to syenogranite with predominant monzogranite and granodiorite. They were possibly formed in an island-arc setting. A younger post-collisional assemblage (590–565 Ma) mainly includes the Akash granitic pluton and Aja Mountain granitic batholiths. The granitic Aja Mountain with an elevation of ~1535 m is the most common geological feature of the Hail region, extending in a NE–SW direction. It is a pear-shaped massif pluton and borders Hail city from the west. Regionally, the older intrusive sequence constitutes part of a large, heterogeneous and locally remobilized intrusive assemblage extending ~50 km SW of the Hail region (Kellogg, 1983). A recent geochronological study by Robinson *et al.* (2015*a*,*b*) distinguished four magmatic groups in the Arabian Shield of Saudi Arabia: (1) ~870–675 Ma island-arc and syn-orogenic I-type magmatism, (2) ~640–585 Ma I- and A-type magmatism, (3) ~610–600 Ma post-orogenic A-type magmatism, and (4) <600 Ma anorogenic A-type magmatism. Accordingly, the older magmatic assemblage in the Hail region is generally equivalent to groups 1 and 2. The local report of Kellogg & Stoeser (1985) suggested that the studied Gabal Samra and Gabal Abd gabbros belong to the orogenic assemblage (>620 Ma), and were considered as metagabbros. It is important to note that the stratigraphic nomenclature in the local report of Kellogg & Stoeser (1985) was preliminary and has not been confirmed by petrological and geochemical studies. Interestingly, a similar scenario occurred for the Sinai mafic magmatism, where the post-collisional gabbroic intrusions were mapped and considered as metagabbros (Khalil *et al.* 2015). In general, the metagabbros were formed during the Cryogenian period (~850–780 Ma) as arc- and collisional-related intrusions, whereas the younger fresh gabbros such as the studied Samra and Abd gabbros were formed as post-collisional intrusions during the Ediacaran period (~620–590 Ma) in the late stages of arc amalgamation in the Arabian Shield (Johnson *et al.* 2011, 2013; Surour *et al.* 2017). The metagabbros were formed during a period of regional metamorphism, which must pre-date the unmetamorphosed younger fresh gabbros (e.g. Surour *et al.* 2017). Mineralogical characteristics (i.e. presence of primary olivine, pyroxene, plagioclase, amphibole and biotite with scarcity of altered mineral phases) of the studied gabbros are typical of unmetamorphosed mafic rocks. Geological field studies and geochemical data on the basement rocks of the Arabian and Nubian Shield indicate that the younger post-collisional gabbros were intruded by post-collisional A-type granitic rocks (i.e. alkali feldspar granite, alkaline granite, monzogranite, syenogranite and syenite) (Khalil *et al.* 2015; Surour *et al.* 2017; Abdallah *et al.* 2020). Field relations clearly show that the studied gabbros were intruded by post-collisional A-type monzogranite and syenogranite (Fig. 1b, c). Accordingly, the geological and mineralogical characteristics are typical of the younger post-collisional gabbros. Moreover, the geochemical data of the present study support emplacement in a post-collisional regime.

https://doi.org/10.1017/S0016756821000182 Published online by Cambridge University Press

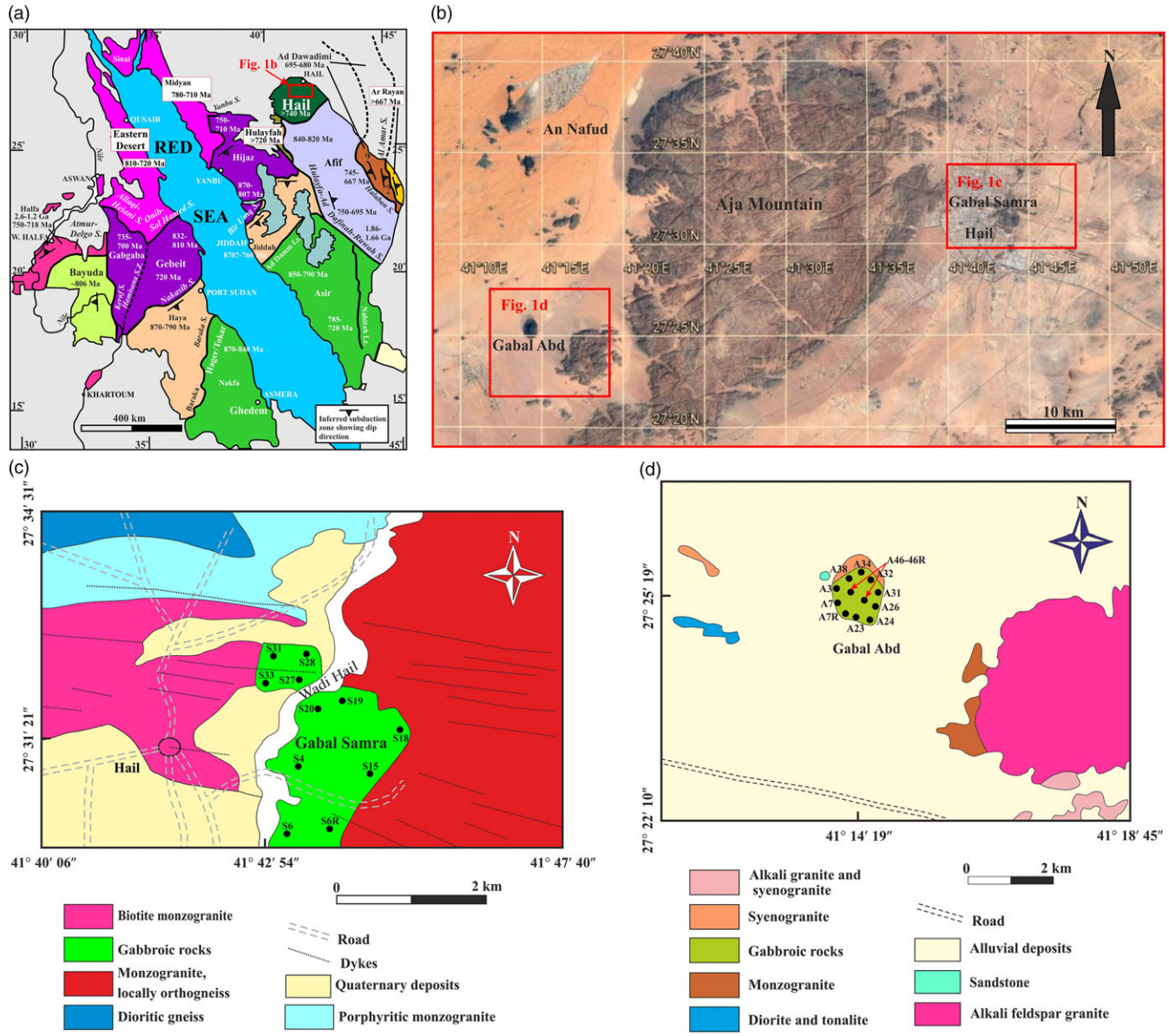

Fig. 1. (Colour online) (a) Location of the Hail region within the Arabian–Nubian Shield (ANS) terrains (Johnson & Woldehaimanot, 2003). (b) Google Earth photo shows location of the Gabal Samra and Gabal Abd within the Hail region (map data: Google, Landsat/Copernicus). Simplified geological maps (modified after Ekren *et al.* 1987) show (c) Gabal Samra, and (d) Gabal Abd. Sample locations are shown. Location of (b) is indicated in (a), and similarly location of (c, d) is indicated in (b).

The mafic intrusions of Gabal Samra occur to the east of Aja Mountain, whereas those of Gabal Abd occur to the southwest (Fig. 1b). No xenoliths were recorded in the studied gabbroic rocks. We collected a total of 23 rock samples for petrographic study and geochemical analysis. This included 11 samples from Gabal Samra and 12 samples from Gabal Abd. The distribution and location of the collected samples are shown in Figure 1c, d.

2.a. Gabal Samra

Gabal Samra is a prominent black mountain located directly east of Hail city (Fig. 1b, c) and consists of a suite of intrusive rocks. The Samra intrusive suite (Fig. 1c) comprises gabbro with monzogranite and dioritic gneiss. Based on the present field study, the Samra gabbro is intrusive and shows a contact with the country rocks (i.e. sharp intrusive contact) that is consistent with the younger variety of gabbro. Moreover, this study shows that the samples have petrographic, mineralogical and geochemical characteristics of the younger fresh gabbro. Gabal Samra occurs as moderate- to low-relief conical-shaped intrusions (Fig. 2a), covering about 3 km^2. The Samra gabbros are fresh, massive, black to dark grey (Fig. 2b), and medium- to coarse-grained rocks. They are intruded by monzogranite (Fig. 1c) and by mafic and felsic dyke swarms (Fig. 2c) and are characterized by quartz- and pegmatite-veins (Fig. 2b). Some gabbroic varieties are locally foliated and intruded by dolerite dykes (Fig. 2d). Many of the mafic dykes cutting the gabbroic rocks are strongly foliated. The width of the dykes reaches up to several metres.

The predominant granitic rocks in the Samra area comprise biotite monzogranite, porphyritic monzogranite and locally gneissose monzogranite. They are mainly massive, pale pink to greyish pink in colour, medium- to coarse-grained and hypidiomorphic to

https://doi.org/10.1017/S0016756821000182 Published online by Cambridge University Press

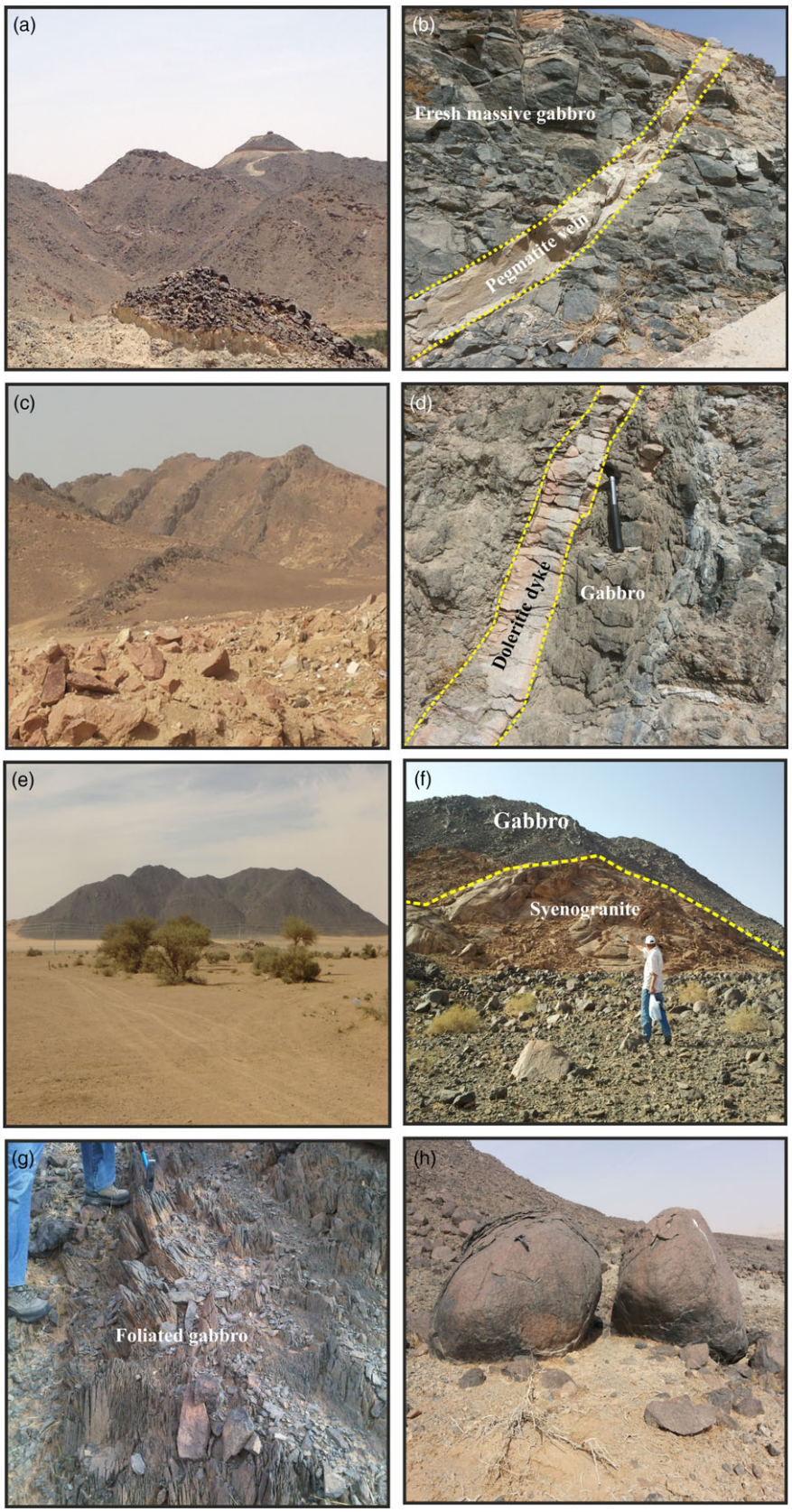

Fig. 2. (Colour online) Field photographs of (a–d) Samra and (e–h) Abd showing (a) general view of Gabal Samra exhibiting conical-shaped intrusions; (b) close-up view of fresh massive gabbro with pegmatite vein; (c) felsic dyke swarms dissecting gabbro; (d) dolerite dyke invading foliated gabbro; (e) general view of Gabal Abd displaying isolated, elongated gabbro masses surrounded by sand dunes and alluvial deposits; (f) intrusion of syenogranite into gabbroic rocks; (g) foliated gabbroic rocks; (h) exfoliation and boulder weathering of gabbroic rocks. Hammer for scale is ˜30 cm in length.

https://doi.org/10.1017/S0016756821000182 Published online by Cambridge University Press

porphyritic rocks. Porphyritic monzogranites occur several kilometres north of the Hail region and are leucocratic with a characteristic porphyritic texture. Biotite monzogranites show a sharp contact with gabbros in the northeastern part of Hail city. Dioritic gneisses represent the oldest rock unit and cover ~15 km^2 north of Hail city. They are strongly foliated with a well-developed compositional banding and are intruded by porphyritic monzogranite. Numerous mafic to felsic dykes (up to ~400 m width) intruded these granitic rocks.

2.b. Gabal Abd

Gabal Abd is located southwest of the Aja Mountain granitic rocks and Hail region (Fig. 1b). Its intrusive suite (Fig. 1d) comprises alkali feldspar granite, syenogranite, monzogranite and diorite along with gabbroic rocks. The gabbroic intrusions occur as isolated, large elongated masses surrounded by sand dunes and alluvial deposits (Fig. 2e). Alkali feldspar granites form a large intrusion covering the southeastern part of the study area along with small bodies of monzogranite, alkali granite and syenogranite (Fig. 1d). Also, small intrusions of diorite and tonalite with syenogranite occur to the west of Gabal Abd (Fig. 1d). The alkali feldspar granites are the most common A-type granitic rocks in the study area. They are medium- to coarse-grained rocks with a characteristic pink colour and massive appearance. The syenogranites belong to A-type granitic rocks and show a pink to yellowish pink colour with a medium- to coarse-grained and hypidiomorphic appearance. They intruded the Abd gabbroic rocks (Fig. 2f). The monzogranites are pale pinkish in colour, medium grained and mainly hypidiomorphic.

There are no any previous studies on the Abd gabbroic rocks. Based on the field observations, the gabbroic rocks were intruded by syenogranite (Fig. 2f) with a sharp intrusive contact. They are fresh, massive rocks with a greenish dark colour and are medium to coarse grained. Also, mafic and aplite dykes together with quartz-veins cut through the gabbroic complex. The veins and dykes range from a few centimetres to several metres in width. In some places, strongly foliated gabbro is present (Fig. 2g), probably related to regional shear zones of the Najd Fault System. The gabbroic rocks show exfoliation and boulder weathering (Fig. 2h). The boulder weathering is also observed in the other younger fresh gabbros from the Arabian Shield (Surour *et al.* 2017). Hybrid rocks are commonly observed along the contact between the granite and gabbro indicating that they represent part of the same magmatic suite. Generally, coarse-grained to pegmatitic mesocratic to leucocratic gabbros are also observed.

3. Petrography

Overall, both the Samra and Abd mafic intrusions are composed of similar gradational varieties of gabbros (i.e. olivine, pyroxene-amphibole and anorthositic gabbros) with comparable petrographic features. The gabbroic rocks show a melanocratic to mesocratic colour index. They are composed mainly of plagioclase, pyroxene and amphibole with subordinate olivine and biotite. Accessory minerals are represented by opaque minerals (chromite, sulfides and Fe–Ti oxides), apatite and titanite. Minor serpentine and chlorite are present as secondary constituents. The common texture is hypidiomorphic-granular (Fig. 3a). Moreover, the rocks show evidence of ophitic to sub-ophitic, intergranular and cumulate textures (Fig. 3).

Olivines form fresh rounded to sub-rounded grains and show slight iddingsite alteration along cracks. Sometimes, olivine phenocrysts are rimmed by pyroxene forming a corona structure (Fig. 3b). Pyroxenes are mainly clinopyroxene (diopside, augite and minor pigeonite) with scarce orthopyroxene (enstatite). Clinopyroxene shows schiller structure (Fig. 3c), which is characteristic of layered and discordant intrusions. This schiller structure is not exsolved ortho- or clinopyroxene, but is composed of very small rods of black opaque minerals (i.e. possibly magnetite). Plagioclase occurs as coarse prismatic crystals forming a cumulate texture (Fig. 3d) and as lath-shaped crystals with well-developed lamellar twinning and occasional compositional zoning. Plagioclase can be partially or totally enclosed by clinopyroxene, developing sub-ophitic and ophitic textures (Fig. 3e). The mafic minerals (e.g. pyroxene and amphibole) fill the angular interstices between the plagioclase crystals, forming an intercumulus texture (Fig. 3f). Amphibole and biotite are found as interstitial phases (Fig. 3g). Amphibole is a green variety and occurs as platy and prismatic crystals (Fig. 3a, g). Occasionally, simple twinning is observed in the amphiboles. Plagioclase interstices are filled with intercumulus amphibole (Fig. 3h). Biotite is yellowish brown, and is found as prismatic phenocrysts and as shred-like crystals with perfect cleavage in one direction (Fig. 3a, g). It exhibits parallel extinction and characteristic bird's eye texture during extinction (Fig. 3a). Fine euhedral apatite crystals occur as inclusions in biotite. Opaque minerals comprise chromite, sulfides and Fe–Ti oxides. Generally, chromite is formed earlier and most probably as a cumulus phase. The sulfides and Fe–Ti oxides are present as interstitial (intercumulus) phases (Fig. 3d).

4. Analytical methods

Microprobe analyses of different mineral phases (online Supplementary Material Tables S1–S10) were performed with a JEOL JXA8200 electron microprobe at the Faculty of Earth Sciences, King Abdulaziz University, Jeddah, Saudi Arabia. The conditions of the electron beam were 15 keV accelerating voltage, 20 nA probe current, 3 μm beam diameter and 20 s counting time for each element. The analytical results were corrected using the ZAF method. Ferric and ferrous iron in amphibole was stoichiometrically estimated with the Gualda & Vlach (2005) method. The analyses were carried out using different standards: ferrohornblende for Si and Al; eskolaite for Cr (99.99 wt % Cr_2O_3); periclase for Mg; wollastonite for Ca; fayalite for Fe; nickel oxide for Ni (99.99 wt % NiO); $KTiPO_5$ for K and Ti; jadeite for Na; and manganosite for Mn. In rare cases, quartz and corundum were used as standards for Si and Al, respectively.

Twenty-three representative rock samples were analysed for major oxides, trace elements and rare earth elements (REEs) (Table 1) at the Department of Geology, Northwest University, China. Major elements were analysed using 0.7 g sample powders mixed with 3.6 g $Li_2B_4O_7$, 0.3 g LiF, 0.4 g NH_4NO_3 and two to three drops of 1.5 % (w/w) LiBr solution. The mixtures were put into platinum (Pt 95 % + Au 5 %) crucibles, and melted in a high-frequency melting instrument into glass beads then analysed by X-ray fluorescence (XRF) (Rigku RIX2100). Trace elements and REEs were analysed using 50 mg sample powders digested using HNO_3, HF and $HClO_4$ in polytetrafluoroethylene (PTFE) bombs with steel sleeves heated with an electronic oven at 190 °C for 48 hours. The final solutions were diluted to 80 g using 2 % HNO_3 with internal standard (10 ng/g Rh in the solution) and analysed using an inductively coupled plasma mass spectrometer (ICP-MS) (Agilent 7500a). USGS rock standard (BCR-2, BHVO-1 and AVG-1) analyses show a precision and accuracy better than

https://doi.org/10.1017/S0016756821000182 Published online by Cambridge University Press

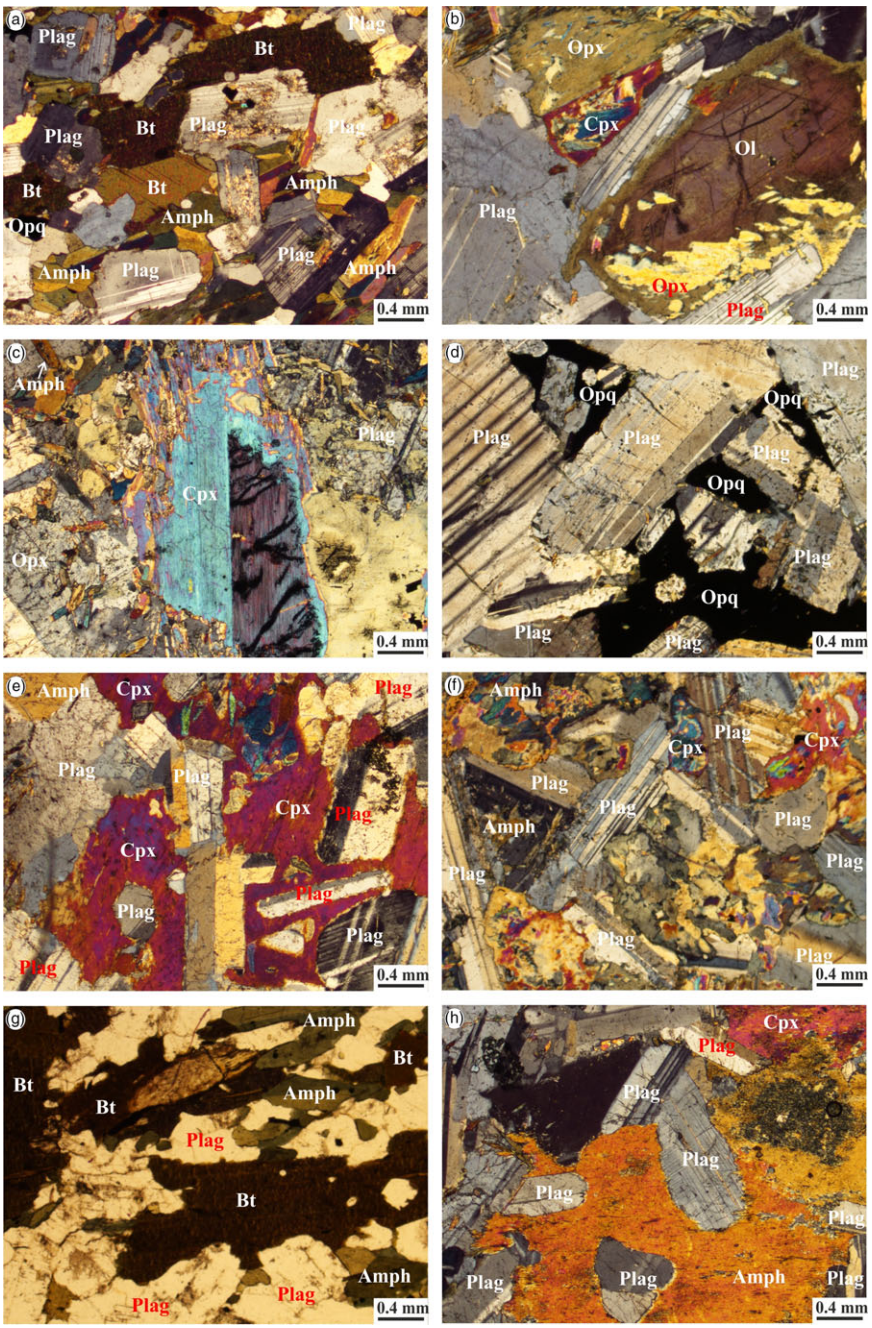

Fig. 3. (Colour online) Photomicrographs showing petrography, mineralogy and textures of the studied gabbros. (a) Hypidiomorphic-granular texture. Some amphibole crystals show twinning. (b) Olivine phenocryst rimed by pyroxene corona. (c) Simple twinned clinopyroxene with schiller structure. Slight amphibole rim grows around pyroxene. (d) Cumulate plagioclase texture with interstitial opaque minerals. Some plagioclase crystals show signs of deformation. (e) Plagioclase crystals enclosed within pyroxene forming ophitic textures. Minor alterations are observed in plagioclase. (f) Intergranular texture. (g) Interstitial amphibole and biotite. (h) Plagioclase crystals with interstitial amphibole. All under crossed nicols except (g). Abbreviations: Ol – olivine; Opx – orthopyroxene; Cpx – clinopyroxene; Plag – plagioclase; Amph – amphibole; Bt – biotite; Opq – opaque minerals.

5 % for major elements and 10 % for trace elements. For details of sample preparation, we refer to Kun *et al.* (2014).

5. Results

5.a. Mineral chemistry

The mineral chemistry of various phases reflects parental magma compositions and crystallization history conditions. Chemical compositions and structural formulas of silicate (olivine, plagioclase, pyroxene, amphibole, biotite, titanite, serpentine) and opaque (chromite, sulfides, Fe–Ti oxides) minerals are listed in online Supplementary Material Tables S1–S10.

Olivine compositions are enriched in MgO (31.5–44.1 wt %; online Supplementary Material Table S1), indicating the relatively primitive nature of their parental mafic magma. They have a relatively wide range of $Fo_{63.54–82.23}$ contents, suggesting normal magma fractionation of different olivine generations. They overlap those of younger gabbros from the ANS as well as gabbroic intrusions from Bushveld and Skaergaard (Fig. 4a).

https://doi.org/10.1017/S0016756821000182 Published online by Cambridge University Press

Table 1. Major, trace- and rare earth elements of the studied gabbros

Area	Samra											Abd											
Sample No.	S4	S6	S6R	S15	S18	S19	S20	S27	S28	S31	S33	A3	A7	A7R	A23	A24	A26	A31	A32	A34	A38	A46	A46R
Major oxides (wt %)																							
SiO_2	49.57	47.56	47.63	47.53	47.23	48.11	47.17	46.67	46.59	46.33	48.25	49.61	47.31	47.49	47.60	48.47	47.44	46.07	45.98	47.60	48.09	46.44	46.50
TiO_2	0.21	0.32	0.31	0.16	0.11	0.35	0.21	0.10	0.17	0.35	0.35	0.27	0.53	0.54	0.22	0.64	0.53	0.48	0.41	0.51	0.39	0.28	0.29
Al_2O_3	28.66	19.91	19.89	20.07	24.27	15.53	20.77	24.95	20.08	26.10	12.77	25.41	19.49	19.58	9.66	15.64	23.19	19.95	23.20	23.56	25.73	25.49	25.42
$Fe_2O_3^t$	2.64	7.31	7.31	4.97	3.93	5.97	5.05	3.92	5.19	4.74	5.71	3.45	6.61	6.58	9.23	8.85	5.82	8.16	6.97	5.92	4.11	4.90	4.94
MnO	0.04	0.11	0.11	0.09	0.07	0.11	0.09	0.06	0.09	0.07	0.12	0.06	0.11	0.11	0.16	0.14	0.09	0.11	0.09	0.09	0.06	0.06	0.06
MgO	1.60	8.53	8.53	9.40	6.02	11.57	7.94	5.82	9.83	4.13	11.63	3.38	8.79	8.77	13.80	9.28	5.11	9.10	7.40	4.89	3.58	4.58	4.62
CaO	12.84	11.66	11.66	14.85	14.78	15.63	15.46	14.89	15.48	15.43	16.84	13.36	13.03	13.02	14.39	12.86	13.20	12.44	11.96	11.76	13.95	12.50	12.50
Na_2O	3.18	2.43	2.40	1.09	1.64	0.94	1.43	1.68	1.20	1.49	1.21	2.67	1.83	1.84	1.16	2.15	2.67	1.83	2.08	3.04	2.48	2.40	2.42
K_2O	0.12	0.16	0.15	0.35	0.10	0.27	0.07	0.06	0.10	0.15	0.30	0.27	0.32	0.33	0.14	0.14	0.13	0.21	0.21	0.27	0.18	0.56	0.56
P_2O_5	0.03	0.06	0.06	0.01	0.01	0.03	0.01	0.01	0.01	0.01	0.01	0.03	0.13	0.12	0.04	0.04	0.12	0.06	0.07	0.06	0.06	0.03	0.03
LOI	0.74	1.48	1.46	1.27	1.40	1.08	1.32	1.39	0.77	0.92	2.52	1.26	1.36	1.34	3.10	1.36	1.23	1.20	1.20	2.03	0.96	2.36	2.35
Total	99.63	99.53	99.51	99.79	99.56	99.59	99.52	99.55	99.51	99.72	99.71	99.77	99.51	99.72	99.50	99.57	99.53	99.61	99.57	99.73	99.59	99.60	99.69
Mg no.	54.57	69.82	69.82	78.96	75.24	79.36	75.72	74.65	78.98	63.34	80.17	66.02	72.51	72.55	74.78	67.52	63.51	68.86	67.80	62.09	63.33	64.95	64.96
Trace elements (ppm)																							
Li	1.87	6.99	7.25	12.83	4.74	2.87	3.41	2.42	2.80	3.48	12.37	3.03	3.39	3.51	9.88	2.28	2.68	2.46	2.87	8.97	2.03	10.50	10.59
Be	0.34	0.18	0.18	0.11	0.11	0.14	0.09	0.10	0.08	0.21	0.13	0.32	0.28	0.28	0.16	0.25	0.30	0.33	0.32	0.35	0.28	0.38	0.39
Sc	6.82	31.84	31.15	48.06	24.05	93.77	46.37	23.11	44.58	24.78	22.58	24.60	66.14	64.21	2.69	68.93	25.01	56.11	18.44	17.09	20.71	13.61	14.10
V	61.15	114.6	115.9	109.5	71.3	167.3	124.5	64.1	105.3	173.2	210.6	69.2	150.1	147.8	249.0	186.8	111.7	136.3	75.11	111.5	82.09	58.19	59.31
Cr	19.36	158.4	160.0	265.6	330.3	1382.7	316.4	258.0	614.6	383.5	846.0	119.8	1184.6	1182.0	1289.7	410.4	264.8	1303.5	158.3	193.1	230.9	220.9	226.9
Co	20.53	54.56	55.31	49.27	37.57	49.84	39.42	40.75	49.96	33.67	38.88	48.44	49.64	48.39	53.21	58.38	42.08	55.61	46.96	36.56	39.20	31.61	32.08
Ni	7.14	40.66	41.52	57.62	40.36	149.4	73.32	36.73	98.46	36.82	46.99	11.27	36.80	35.33	124.8	50.76	17.99	80.45	69.60	29.75	17.69	39.24	40.33
Cu	3.48	43.07	44.12	39.96	28.11	83.78	94.64	58.80	86.51	25.99	19.20	5.76	5.14	4.98	50.14	113.9	13.02	3.58	4.03	8.38	21.27	3.01	3.23
Zn	16.54	40.44	40.54	36.15	22.71	37.26	25.51	22.29	26.07	31.56	40.01	21.39	40.68	40.44	43.17	47.20	37.69	64.09	38.64	35.38	22.43	27.18	27.56
Ga	17.95	14.27	14.39	12.65	15.23	10.91	13.79	15.50	12.36	15.46	8.75	17.68	13.52	13.32	7.89	13.89	16.53	14.95	14.82	16.53	17.37	15.96	16.25
Ge	0.71	1.00	1.01	1.16	0.73	1.30	1.08	0.83	1.00	0.91	1.57	0.96	1.07	1.11	1.96	1.40	0.99	1.05	0.88	0.95	0.88	0.75	0.76
Rb	0.85	3.47	3.54	8.51	1.87	3.71	1.73	0.89	2.52	3.16	10.52	5.10	7.22	6.80	2.69	2.48	1.77	4.20	4.27	7.02	4.03	10.55	13.29
Sr	670.4	611.5	616.0	450.2	624.0	342.8	520.6	659.8	419.6	609.3	332.0	633.1	542.7	543.4	173.2	431.1	545.5	504.5	678.9	718.0	605.6	890.1	903.6
Y	2.13	5.81	5.93	4.13	2.59	9.06	4.57	2.46	4.32	4.95	7.92	6.68	9.78	9.61	4.14	10.09	9.43	8.33	7.12	6.59	6.97	4.83	4.88
Zr	3.97	10.93	11.09	6.53	3.19	16.35	5.46	2.82	5.47	6.07	9.13	21.49	11.68	12.24	6.25	15.82	37.81	14.01	13.36	26.20	13.81	15.41	16.40
Nb	0.34	0.36	0.38	0.16	0.07	0.31	0.07	0.05	0.09	0.23	0.19	1.01	0.96	0.98	0.32	0.86	1.09	1.20	1.47	1.24	0.96	0.79	0.70
Cs	0.12	0.30	0.30	0.30	0.10	0.27	0.16	0.05	0.04	0.08	0.69	0.06	0.21	0.21	0.26	0.13	0.07	0.15	0.16	0.28	0.05	0.48	0.51
Ba	70.18	78.93	79.60	76.70	36.88	71.17	30.30	61.01	30.68	41.81	40.87	147.5	62.08	59.95	74.54	80.05	77.98	38.34	46.52	74.91	58.78	95.29	96.52

(*Continued*)

Table 1. (*Continued*)

Area	Samra											Abd											
Sample No.	S4	S6	S6R	S15	S18	S19	S20	S27	S28	S31	S33	A3	A7	A7R	A23	A24	A26	A31	A32	A34	A38	A46	A46R
REEs (ppm)																							
La	1.34	1.85	1.89	0.93	0.79	2.13	0.89	0.81	0.81	1.36	1.07	3.69	1.74	1.70	1.67	2.00	3.39	2.29	2.69	2.88	2.57	2.50	2.65
Ce	3.24	4.50	4.60	2.07	1.86	5.41	2.32	1.85	2.30	3.82	3.27	8.26	4.47	4.38	3.68	5.44	8.61	5.83	6.65	6.91	6.43	5.71	6.00
Pr	0.40	0.67	0.69	0.36	0.27	0.88	0.39	0.28	0.37	0.57	0.58	1.10	0.73	0.72	0.51	0.86	1.25	0.87	0.95	0.95	0.90	0.73	0.76
Nd	1.80	3.38	3.43	1.85	1.39	4.61	2.20	1.39	1.99	2.89	3.33	4.80	4.05	3.98	2.41	4.63	6.10	4.42	4.56	4.44	4.39	3.34	3.46
Sm	0.43	0.96	1.00	0.61	0.43	1.47	0.73	0.42	0.68	0.85	1.20	1.22	1.43	1.41	0.69	1.54	1.72	1.36	1.25	1.18	1.21	0.88	0.88
Eu	0.50	0.56	0.57	0.33	0.37	0.55	0.43	0.37	0.38	0.52	0.46	0.66	0.59	0.58	0.23	0.77	0.73	0.72	0.62	0.78	0.66	0.66	0.67
Gd	0.43	1.07	1.11	0.70	0.49	1.64	0.84	0.46	0.77	0.92	1.41	1.29	1.76	1.73	0.74	1.82	1.86	1.54	1.35	1.25	1.34	0.94	0.94
Tb	0.06	0.17	0.18	0.12	0.08	0.27	0.14	0.08	0.13	0.15	0.24	0.20	0.30	0.30	0.12	0.31	0.29	0.25	0.22	0.20	0.21	0.15	0.15
Dy	0.40	1.08	1.10	0.78	0.51	1.70	0.88	0.47	0.84	0.97	1.57	1.23	1.87	1.88	0.76	1.94	1.79	1.59	1.34	1.24	1.33	0.92	0.91
Ho	0.08	0.21	0.22	0.15	0.10	0.34	0.18	0.10	0.17	0.19	0.32	0.25	0.38	0.38	0.16	0.39	0.35	0.31	0.27	0.24	0.26	0.18	0.18
Er	0.22	0.59	0.61	0.43	0.28	0.95	0.49	0.26	0.47	0.54	0.88	0.69	1.05	1.05	0.46	1.07	0.96	0.87	0.75	0.69	0.73	0.51	0.50
Tm	0.03	0.08	0.09	0.06	0.04	0.13	0.07	0.04	0.07	0.08	0.12	0.10	0.14	0.14	0.07	0.15	0.14	0.12	0.11	0.10	0.10	0.07	0.07
Yb	0.20	0.51	0.53	0.38	0.24	0.82	0.40	0.22	0.39	0.47	0.76	0.62	0.87	0.86	0.45	0.92	0.81	0.75	0.65	0.62	0.64	0.46	0.46
Lu	0.03	0.07	0.08	0.06	0.03	0.12	0.06	0.03	0.06	0.07	0.11	0.09	0.13	0.13	0.07	0.14	0.12	0.11	0.10	0.09	0.10	0.07	0.07
Hf	0.13	0.35	0.36	0.24	0.13	0.58	0.23	0.12	0.22	0.25	0.38	0.63	0.51	0.52	0.23	0.59	0.96	0.51	0.43	0.66	0.45	0.43	0.46
Ta	0.05	0.04	0.04	0.03	0.03	0.05	0.03	0.03	0.03	0.05	0.03	0.15	0.09	0.09	0.03	0.09	0.11	0.10	0.12	0.11	0.12	0.08	0.07
Pb	1.63	1.01	1.02	2.79	2.20	1.44	1.71	1.49	0.77	1.68	1.48	1.44	0.92	0.94	0.78	0.89	1.38	0.55	0.71	1.10	0.80	3.13	3.14
Th	0.06	0.12	0.12	0.07	0.02	0.17	0.02	0.02	0.03	0.02	0.06	0.69	0.11	0.10	0.17	0.14	0.36	0.17	0.19	0.28	0.19	0.27	0.29
U	0.05	0.07	0.07	0.06	0.11	0.17	0.09	0.02	0.03	0.09	0.08	0.25	0.07	0.07	0.11	0.07	0.18	0.08	0.10	0.12	0.09	0.13	0.14

Mg no. = 100*Mg/(Mg + Fe^{2+})

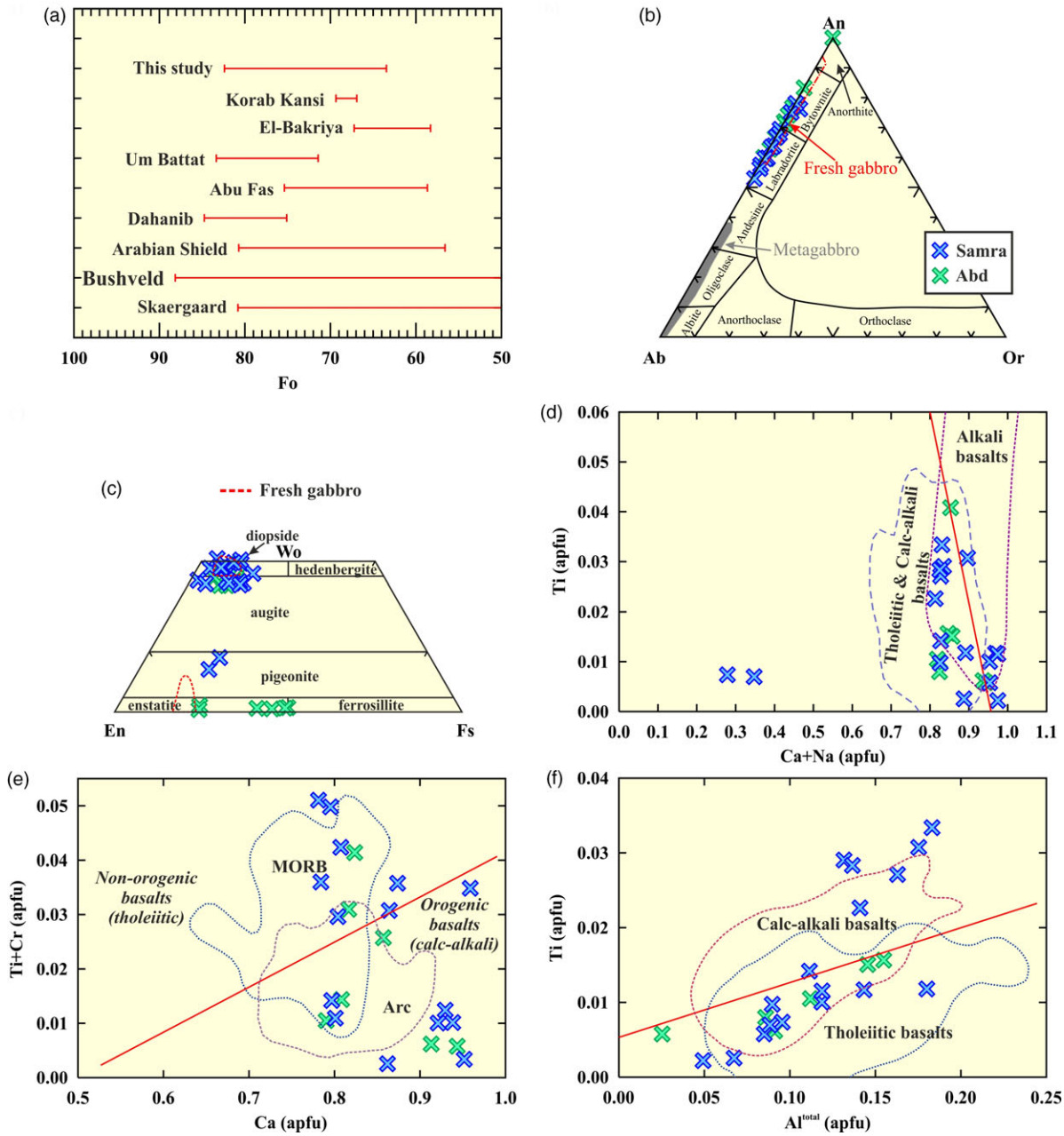

Fig. 4. (Colour online) (a) Olivine compositions compared with those in younger gabbroic intrusions. Data sources: Arabian Shield – Surour *et al.* (2017); Nubian Shield (e.g. Umm Battat, El-Bakryia, Korab Kansi, Abu Fas, Dahanib) – Dixon (1981); M. F. Sadek, unpub. Ph.D. thesis, Ain Shams Univ. (1994); Abdel-Karim *et al.* (2011); Bushveld and Skaergaard intrusions – Wager & Brown (1967). (b) Ab–An–Or ternary diagram for plagioclase (Deer *et al.* 1992). Fields of metamorphosed and fresh gabbros are after Surour *et al.* (2017). (c) Plots of pyroxene compositions on quadrilateral classification diagram (Morimoto *et al.* 1988). Pyroxene compositions from fresh gabbros in Arabian Shield (Surour *et al.* 2017) are shown for comparison. (d) Ti v. Ca + Na, (e) Ti + Cr v. Ca, and (f) Ti v. Al^{total} diagrams after Leterrier *et al.* (1982).

Feldspars are calcic plagioclase (CaO = 10.98–24.90 wt %), ranging from anorthite to labradorite (Fig. 4b) (online Supplementary Material Table S2). They have anorthite contents ($An_{52.92–99.93}$) comparable to those of fresh gabbros from the Arabian Shield and higher than those from metagabbros (Fig. 4b; Surour *et al.* 2017). This range is also similar to that of gabbroic intrusions in the Eastern Desert of Egypt (Abdel Halim *et al.* 2016; Mogahed, 2019).

Pyroxenes comprise both ortho- and clinopyroxene similar to fresh gabbros from the western Arabian Shield (Fig. 4c; Surour *et al.* 2017). Orthopyroxene compositions in the Abd gabbros are classified as enstatite (Fig. 4c) with low CaO contents (<1 wt %; online Supplementary Material Table S3). They have a relatively wide range of enstatite contents (En = 0.50–0.76; online Supplementary Material Table S3). Compared to coexisting clinopyroxene, enstatite shows low Al_2O_3 contents (online Supplementary Material Table S3). Clinopyroxenes range from diopside to augite in Samra and Abd, with minor pigeonite in Samra (Fig. 4c). Their Mg no. values range between 0.69 and 0.96. They have low TiO_2 (mostly <1.0 wt %) and Na_2O (average 0.26 wt %) typical of igneous clinopyroxenes from sub-alkaline rocks (Le Bas, 1962) (online Supplementary Material Table S3).

https://doi.org/10.1017/S0016756821000182 Published online by Cambridge University Press

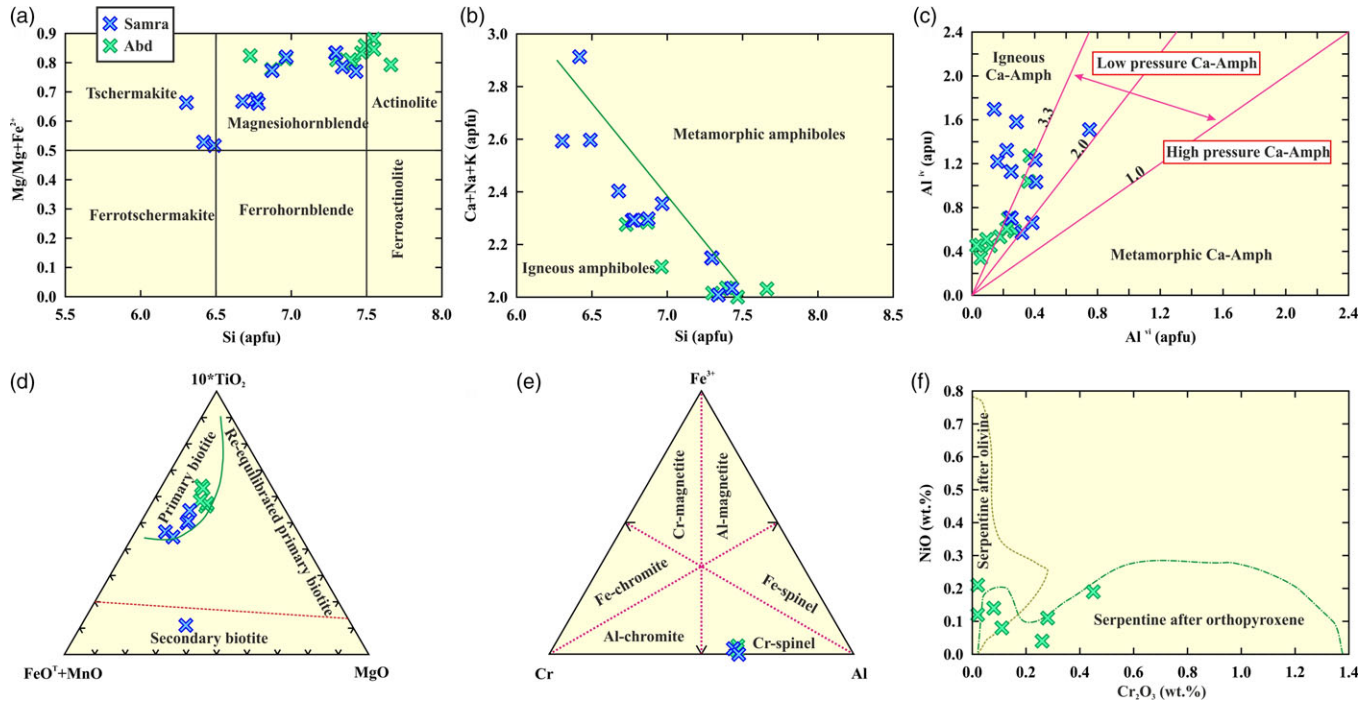

Fig. 5. (Colour online) Amphiboles Si (apfu) compared with (a) Mg/Mg + Fe^{2+} and (b) Ca + Na + K. Amphibole compositional fields are from Leake *et al.* (2004). Igneous and metamorphic amphiboles are after Giret *et al.* (1980). (c) Al^{iv}/Al^{vi} ratio variation in amphiboles structure. Ca-amphiboles of igneous and metamorphic (low- and high-pressure) origin are from Fleet & Barnett (1978). (d) Plot of biotite compositions on FeO + MnO–10*TiO_2–MgO ternary diagram after Nachit *et al.* (2005). (e) Plot of chromite compositions on Cr–Fe^{3+}–Al ternary diagram. (f) Plot of serpentine compositions on NiO–Cr_2O_3 binary diagram after Kodolanyi *et al.* (2012).

Moreover, they show a wide range of compositions extending across those of tholeiitic and calc-alkali basalts (Fig. 4d–f). Generally, the clinopyroxene Mg no. values are comparable to those of fresh gabbroic intrusions in the Eastern Desert of Egypt (Mg no. 0.71–0.86; Abdel Halim *et al.* 2016).

Amphiboles show calcic compositions and are classified mainly as magnesiohornblende with subordinate tschermakite and actinolite (Fig. 5a and online Supplementary Material Table S4). They show variable TiO_2 contents (0.02–3.8 wt %). The Si and Ca + Na + K contents reflect their primary igneous origin (Giret *et al.* 1980) (Fig. 5b). Moreover, the Al^{iv}/Al^{vi} ratios indicate mostly igneous calcic amphiboles, with some analyses showing a low-pressure metamorphic origin (Fig. 5c; Fleet & Barnett, 1978). They have Mg no. values (mostly 0.77–0.90) similar to those for fresh gabbroic intrusions in the Eastern Desert of Egypt (Abdel Halim *et al.* 2016).

Biotites show morphological and optical features (i.e. euhedral crystals, strong brown colour and pleochroism) suggesting a primary nature. Primary magmatic biotites can be discriminated from those of secondary origin using the ternary relationship (FeO + MnO)–10*TiO_2–MgO (Nachit *et al.* 2005). Except for one spot, the analysed biotites from the studied gabbros plot in the field of primary magmatic origin (Fig. 5d). Furthermore, they show physicochemical features reflecting their equilibrium with a magmatic liquid. These features include high TiO_2 (2.6–5.51 wt %) and X_{FeO} (>0.5; $X_{FeO} = (FeO^T/(FeO^T + MgO))$ and the low Al^{vi} (<1) and indicate their primary origin (Nachit *et al.* 2005) (online Supplementary Material Table S5).

Accessory phases comprise chromite, titanite, sulfides and Fe–Ti oxides. Chromite compositions (online Supplementary Material Table S6) are classified as Cr-spinel and plot adjacent to the Cr–Al join (Fig. 5e). They have low Cr no. (37.65–39.28) and Mg no. (34.78–37.01) values similar to those of spinel in fresh layered gabbroic intrusions of the Eastern Desert of Egypt (Abdel Halim *et al.* 2016). Titanite has high TiO_2 (38.75–44.36 wt %) and CaO (26.57–28.74 wt %) with low Al_2O_3, FeO, MnO and MgO concentrations (online Supplementary Material Table S7). Sulfide compositions comprise pyrite and chalcopyrite (online Supplementary Material Table S8). Pyrite shows a wide range of S (36.29–54.06 wt %), Fe (47.33–63.19 wt %) and Cu (0.00–0.53 wt %) contents. Conversely, chalcopyrite has a limited range of S (34.96–35.38 wt %), Fe (30.26–31.15 wt %) and Cu (33.80–34.30 wt %) contents. Fe–Ti oxides are magnetite and ilmenite (online Supplementary Material Table S9). Magnetite has high FeO (87.36–96.41 wt %) and low TiO_2 (0.00–2.87 wt %) contents, whereas ilmenite has high FeO (42.82–51.11 wt %) and TiO_2 (44.41–53.28 wt %) contents. Serpentine represents minor alteration products. It is composed mostly of SiO_2 (42.13–46.30 wt %) and MgO (35.89–41.29 wt %) with low Al_2O_3 (0.31–1.71 wt %) and Cr_2O_3 (0.02–0.45) contents (online Supplementary Material Table S10). The SiO_2 and MgO contents are consistent with the antigorite phase (Wicks & Plant, 1979). Additionally, the Cr_2O_3 and NiO contents indicate serpentine after both olivine and orthopyroxene (Fig. 5f).

5.b. Bulk-rock geochemistry

Major oxides, trace elements and REE abundances of the gabbroic rocks from Gabal Samra and Gabal Abd are listed in Table 1. The gabbroic rocks exhibit a narrow range of SiO_2 contents (45.98–49.61 wt %) with low total alkalis (1.21–3.13 wt %) and plot inside the compositional field of typical gabbros on a total alkali–silica (TAS) diagram (Fig. 6a). They have a sodic nature (Na_2O/K_2O >1). Their Zr/Ti and Nb/Y ratios are typical of sub-alkali basalt (Fig. 6b). According to the Y and Zr contents, they show a tholeiitic character (Fig. 6c). This geochemical feature is in harmony with

https://doi.org/10.1017/S0016756821000182 Published online by Cambridge University Press

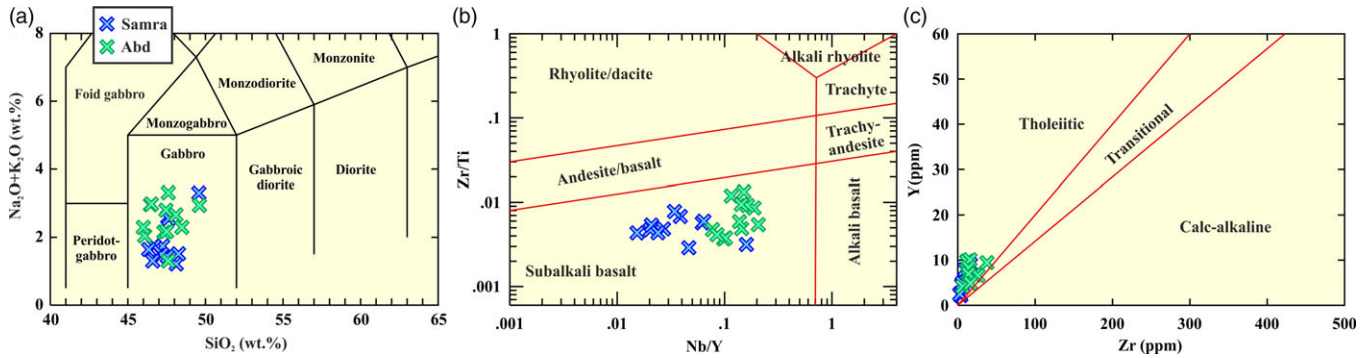

Fig. 6. (Colour online) Chemical nomenclature and classification diagrams for the gabbroic rocks. (a) Total alkalis versus SiO_2 (Middlemost, 1994); (b) Zr/Ti–Nb/Y (Pearce, 1996); (c) Y–Zr (Barrett & MacLean, 1994).

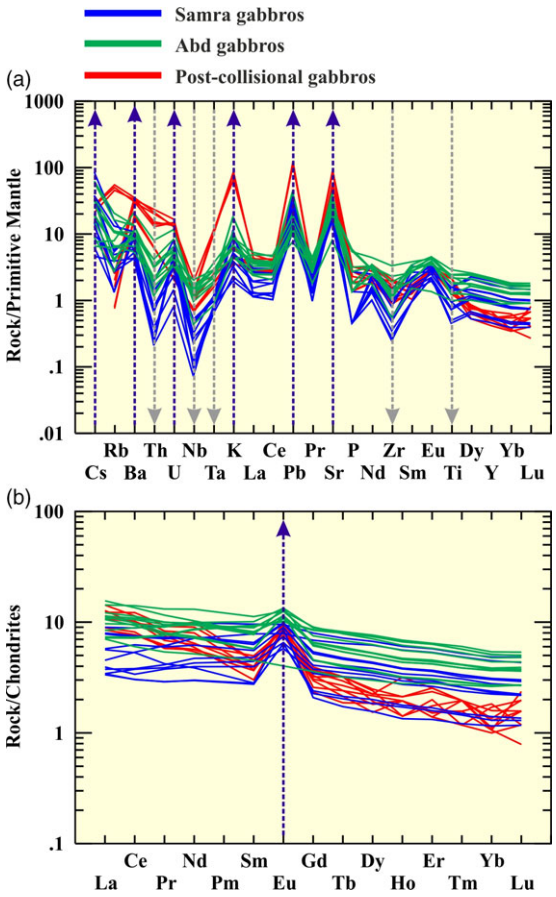

Fig. 7. (Colour online) (a) Primitive mantle-normalized trace-element patterns. (b) Chondrite-normalized REE patterns. Normalization values are from Sun & McDonough (1989). Post-collisional gabbros from the western Arabian Shield (Surour *et al*. 2017) are shown for comparison.

the pyroxene data (Fig. 4d). They show a wide range of Mg no. (54.57–80.17), MgO (1.6–13.8 wt %), Cr (19.36–1383 ppm), Ni (7.14–149.41 ppm) and Sc (2.69–93.77 ppm) contents.

In the primitive mantle-normalized spider diagram (Fig. 7a), the studied gabbros show a depletion of Nb and Ta and enrichment of Pb, Sr, K and U. They display large ion lithophile element (LILE) enrichment (e.g. Cs, Ba, K and Sr) and high-field-strength element (HFSE) depletion (e.g. Th, Nb, Ta, Zr and Ti). In the chondrite-normalized REE patterns, they are enriched in light rare earth elements (LREEs) compared to heavy rare earth elements (HREEs) and show positive Eu anomalies, as do younger fresh gabbros from the western Arabian Shield (Fig. 7b). Generally, their trace-element and REE patterns are comparable to those of younger fresh gabbros from the western Arabian Shield (Fig. 7). They show positive Eu and Sr anomalies together with high Al_2O_3 contents (up to 28.66 wt %). They have low $(Tb/Yb)_N$ values (1.22–1.66).

6. Discussion

6.a. Alteration and crustal contamination effects

The low loss on ignition (LOI) contents (mostly <2.5 wt %) and absence of Ce anomalies (Fig. 7b) of the studied gabbros indicate a negligible effect of alteration (Polat & Hofmann, 2003). Moreover, the Rb/Zr, Sr/Zr, Ba/Zr and Ba/La ratios are not correlated with LOI values, indicating restricted element mobility and an insignificant role of post-magmatic alteration (e.g. Ali & Ntaflos, 2011; Ali *et al.* 2013; Farahat *et al.* 2017; Abdallah *et al.* 2019). The low Th/La ratios (<0.2) along with the negative Zr and Th anomalies suggest insignificant contamination with crustal materials during magma genesis (e.g. Plank, 2005; Yang & Zhou, 2009). The low Th/Nb (average = 0.3) and Th/Ce ratios (average = 0.03) also suggest that the crustal contamination process was insignificant in the genesis of the gabbroic magmas (Taylor & McLennan, 1995; Condie, 2003). Their low Lu/Yb ratios (0.14–0.15) are identical to mantle-derived magmas and lower than continental crust, indicating derivation from a mantle source lacking contamination with continental crust (Sun & McDonough, 1989; Rudnick & Gao, 2003). These inferences are also supported by their low SiO_2 and total REE contents (e.g. Eyuboglu *et al.* 2010; Abdallah *et al.* 2019). Therefore, the bulk-rock compositions reflect a primary geochemical signature and reveal the original nature of their mantle source.

6.b. Magma differentiation and crystallization conditions

The generally sub-parallel chondrite-normalized REE patterns (Fig. 7b) likely reveal that the gabbroic magmas underwent fractional crystallization. Gabbroic samples (S19 and A23) have the highest Mg no., Cr, Co and Ni contents compared to other rock samples, suggesting that they possibly represent the early magmatic products with olivine fractionation from their primary magmas. The wide range of Mg no., Cr, Ni and Sc contents (Table 1) in the studied gabbros are consistent with variable degrees of olivine and pyroxene fractionation. The broad correlations between MgO

https://doi.org/10.1017/S0016756821000182 Published online by Cambridge University Press

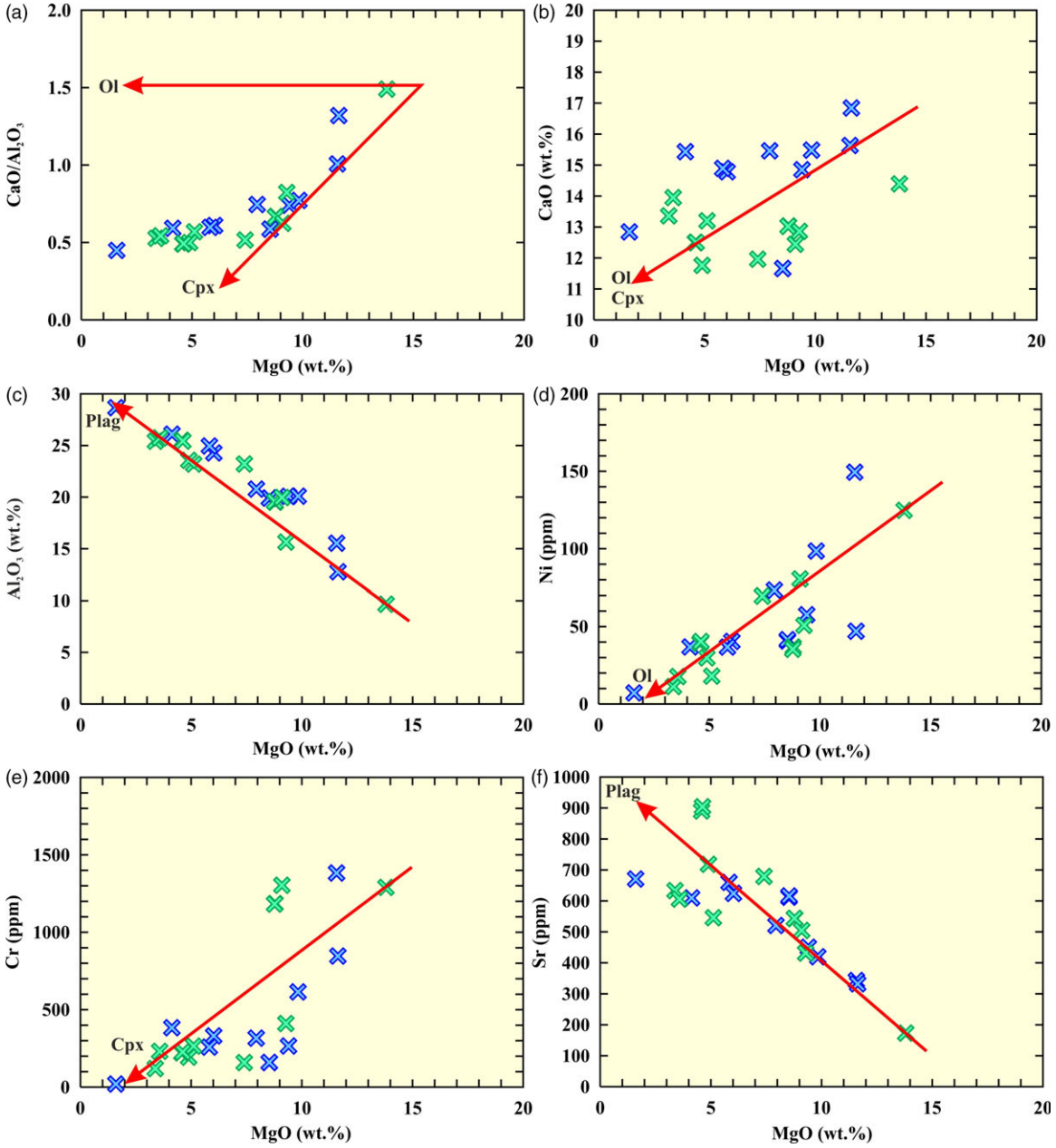

Fig. 8. (Colour online) MgO versus (a) CaO/Al_2O_3, (b) CaO, (c) Al_2O_3, (d) Ni, (e) Cr, and (f) Sr plots to show the possible fractional phases of the studied gabbros during magmatic evolution.

and CaO/Al_2O_3 and CaO (Fig. 8a, b) indicate that they have experienced significant fractionation of olivine and clinopyroxene. This is supported by the positive correlations between MgO and Ni and Cr (Fig. 8d, e). The increase of Al_2O_3 and Sr with decreasing MgO (Fig. 8c, f) probably indicates plagioclase accumulation. Furthermore, the positive Eu and Sr anomalies (Fig. 7) confirm a role of plagioclase accumulation during the evolution of the studied gabbros.

Based on the empirical model of Sack & Ghiorso (1991), the crystallization temperature of the Cr-spinel in the studied gabbros approximates 1050 °C (Fig. 9a). Amphibole crystallization pressure ranges from 3.54 to 7.75 kbar (Schmidt, 1992), comparable to that of layered mafic intrusions from southern Sinai (4.8–6.8 kbar; Azer *et al.* 2016). They crystallized at high oxygen fugacity conditions (fO_2) (Fig. 9b), similar to layered gabbros in southern Sinai (Azer *et al.* 2016). The biotite compositions of the Abd gabbros contain higher MgO (11.32–13.05 wt %) and TiO_2 (4.01–5.51 wt %) contents compared to those of the Samra gabbros, likely suggesting early crystallization at a higher temperature.

6.c. Mineralogical implications

The existence of amphiboles of primary igneous origin in the studied gabbros is consistent with the hydrous nature of the parental magma(s). This is also supported by the presence of primary biotites. Moreover, the occurrence of An-rich plagioclases ($An_{52.92–99.93}$) suggests that their primary melts were Na-depleted and Al- and H_2O-enriched, because plagioclase crystallization under hydrous

https://doi.org/10.1017/S0016756821000182 Published online by Cambridge University Press

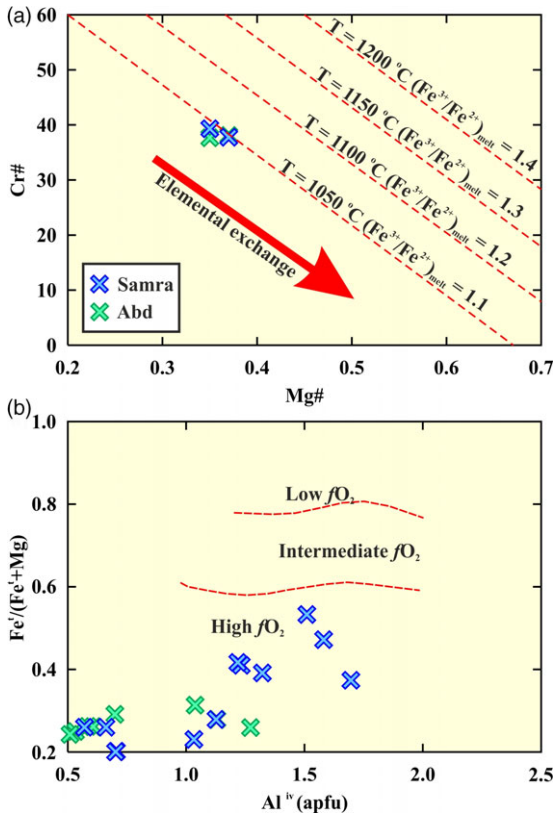

Fig. 9. (Colour online) (a) Cr-spinel empirical thermometer (after Sack & Ghiorso, 1991). Equipotential curves and Fe^{3+}/Fe^{2+} of melt are from Irvine (1965) and Agata & Adachi (2014). The equipotential curves shifting towards the left represents magmatic differentiation, whereas the parallel arrow shows the elemental exchange trend. (b) $Fe^t/(Fe^t + Mg)$–Al^{iv} diagram for amphiboles (Anderson & Smith, 1995).

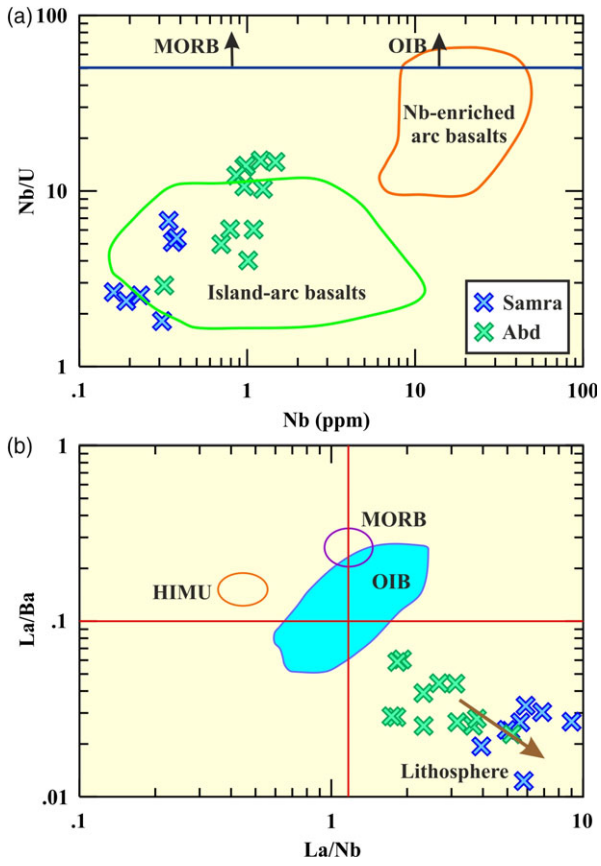

Fig. 10. (Colour online) (a) Nb/U–Nb diagram. Fields for island-arc basalts and Nb-enriched arc basalts are from Defant *et al.* (1992) and Schiano *et al.* (1995), respectively. (b) La/Ba–La/Nb diagram. Ocean-island basalt (OIB), mid-ocean ridge basalt (MORB) and HIMU (high-U/Pb) mantle source fields are from Saunders *et al.* (1992).

conditions leads to increasing An contents (e.g. Carmichael *et al.* 1974; Sisson & Grove, 1993; Panjasawatwong *et al.* 1995; Martel *et al.* 1998; Koepke *et al.* 2004). Their Ca-rich nature (online Supplementary Material Table S2) likely reflects their crystallization from arc-like magmas (Ballantyne, 1992). The clinopyroxene and spinel compositions (Fig. 12) also show an arc-like character. The clinopyroxene (up to Wo_{51}) and olivine (up to $Fo_{82.23}$) compositions suggest crystallization of these minerals from mafic magmas under hydrous conditions (Kushiro, 1990; Kushiro & Mysen, 2002; Mysen, 2014). The gabbroic rocks contain augite and pigeonite characteristic of tholeiitic suites (Fodor & Keil, 1979). Moreover, the pyroxene data indicate a mainly tholeiitic character (Figs 4f, 11a). These implications reflect crystallization from hydrous, mainly tholeiitic, mafic magmas with arc-like signatures, which were probably inherited from the previous subduction process in the ANS.

6.d. Nature of the mantle source and melting conditions

The identical chondrite-normalized REE patterns of the studied gabbros reflect their derivation from a common mantle source. The rocks show low Nb, Ta, Zr and Hf concentrations and subchondritic Nb/U (average = 6.46), Nb/Ta (average = 7.79) and Zr/Hf ratios (average = 29.08), revealing mantle source depletion by a former melt extraction event (e.g. Jochum *et al.* 1986; Yang & Zhou, 2009).

The HREE contents in mafic magmas can be used to constrain mantle melting depths (e.g. Blundy *et al.* 1998; Walter, 1998; Tang *et al.* 2006). The relatively low HREE contents of the studied gabbros (e.g. $Yb_N = 1.18–5.41$) suggest residual garnet in their mantle source (Tang *et al.* 2006). The $(Gd/Yb)_N$ ratios greater than unity indicate garnet in the residue (Walter, 1998). So, the high $(Gd/Yb)_N$ ratios (1.36–1.90) confirm the garnet signature in the mantle residue. Moreover, high ratios of $(Dy/Yb)_N = 1.13–1.48$ indicate that the gabbroic melts were produced from a garnet-peridotite source (Blundy *et al.* 1998). The presence of garnet as a residual phase in the source region requires a melting depth exceeding ~70–80 km at the garnet stability field (Tang *et al.* 2006). This HREE signature suggests a relatively deeper origin for the gabbroic rocks.

6.e. Modification of the mantle source

The geological field relations of the studied gabbros are consistent with post-collisional mafic magmatism. The trace-element and REE patterns (Fig. 7) are also similar to post-collisional mafic rocks. However, the mineralogical and geochemical data show arc-like features (Figs 10a, 11, 12), suggesting that their arc- and subduction-like signatures were probably inherited from the previous collisional stage in the ANS (e.g. Khalil *et al.* 2015; Gahlan *et al.* 2018).

A mantle peridotite source modified by subduction components is widely agreed for the post-collisional magmatism (e.g. Bonin, 2004; Khalil *et al.* 2015; Surour *et al.* 2017; Gahlan *et al.* 2018; Farahat & Ali, 2019). Subduction input raises contents of mobile elements (LILEs; Cs, Rb, Ba, U, K, Pb and Sr) and volatiles

https://doi.org/10.1017/S0016756821000182 Published online by Cambridge University Press

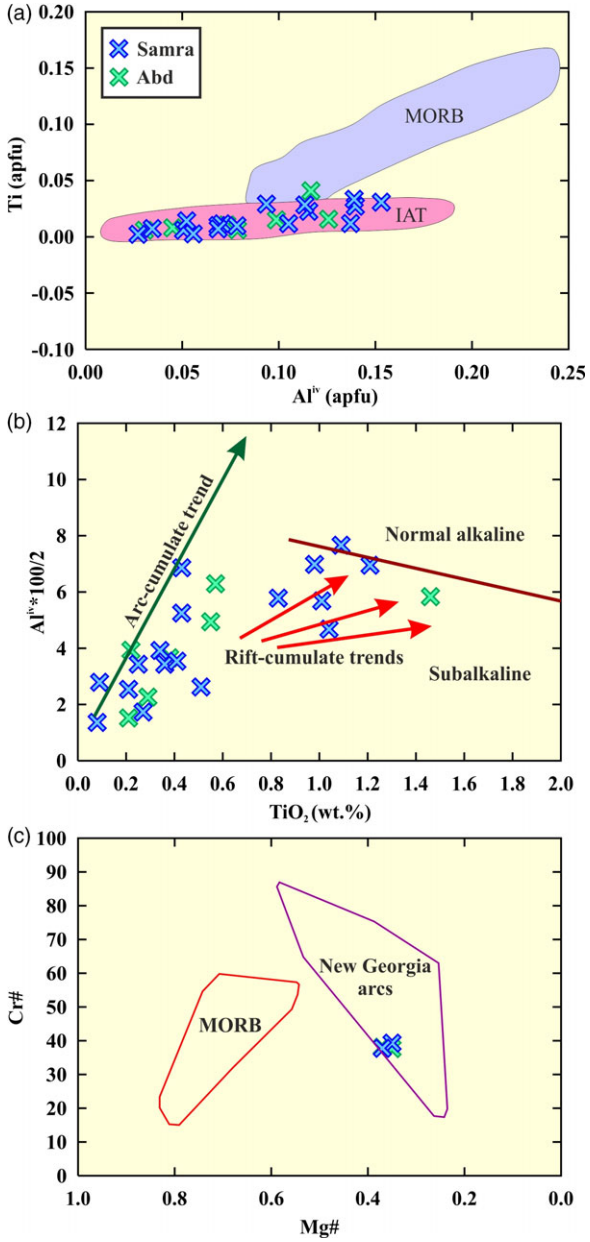

Fig. 11. (Colour online) Pyroxene compositions plotted on (a) Ti v. Al^{iv} diagram (Beccaluva *et al.* 1989) and (b) Al^{iv}*100/2 v. TiO$_2$ diagram. The arc- and rift-cumulate trends are from Loucks (1990). (c) Cr no. v. Mg no. for the studied spinels compared to spinels from the subduction-related magmatic rocks (New Georgia arcs; Ramsay *et al.* 1984) and MORB (Sigurdsson & Schilling, 1976; Dick & Bullen, 1984). Abbreviations: IAT – island-arc tholeiite; MORB – mid-ocean ridge basalt.

(i.e. H_2O, Cl and S) (e.g. Hawkesworth *et al.* 1993; Wallace, 2005). On the other hand, immobile elements (HFSEs; Nb, Ta, Zr, Hf and Y) remain in the subducted slab, leading to their depletion compared to LILEs (Prouteau *et al.* 2001; Bonin, 2004). Accordingly, the LILE enrichment and the HFSE depletion (Fig. 7a) indicate subduction-like signatures. Moreover, these characters are similar to other late Neoproterozoic post-collisional mafic magmatism in the ANS (Khalil *et al.* 2015; Surour *et al.* 2017; Gahlan *et al.* 2018; Farahat & Ali, 2019). The low HFSE content likely reflects the contribution of an arc-related source, and the high LILE content probably reveals that subducted oceanic sediment was also involved in their petrogenesis (Eyuboglu *et al.* 2016). The fluid mobile element (FME; such as Cs, U, Pb and Sr) enrichments (Fig. 7a), and the high Ba/Th (796), Ba/La (38) and Ba/Nb (232) average ratios support the signatures of sediment-derived fluids, which were inherited from the previous subduction event (Cisterna *et al.* 2017; Abdel-Karim *et al.* 2018 and references therein). The La/Nb ratios (>1.4) also reflect subduction-like signatures (Condie, 2003 and references therein), as do the Nb/U ratios, which are consistent with arc-like basalts (Fig. 10a).

Oceanic basalts show relatively elevated and invariable Nb/U ratios (Hofmann *et al.* 1986; Hofmann, 1997). Numerous continental flood basalts conversely show low Nb/U and Nb/La ratios, as do the studied gabbros. This Nb fractionation could happen through melt–rock reactions during asthenospheric magma ascent through the lithospheric mantle due to the different reaction rates of minerals in metasomatized peridotite (Arndt & Christensen, 1992). So, the low Nb/U and Nb/La ratios and negative Nb anomalies of the studied gabbros might indicate contributions of metasomatized lithospheric mantle into their asthenospheric source through a melt–rock reaction process (e.g. Tang *et al.* 2006). This inference is further supported by the relationship between the La/Ba and La/Nb ratios (Fig. 10b), which shows deviation of the studied gabbros from oceanic basaltic melts produced from an asthenospheric source towards lithospheric mantle. So, this trend shown by the studied rocks (Fig. 10b) might also reflect that asthenosphere-derived magmas interacted with lithospheric mantle. We suggest that the gabbroic parental magmas were derived from adiabatic decompression melting of a depleted asthenospheric mantle interacting during ascent with metasomatized lithospheric mantle.

6.f. Geotectonic setting

Geological field study and mineralogical data indicate that the studied gabbros are generally unmetamorphosed and undeformed. Moreover, field relations show that they are intruded by younger monzogranite and syenogranite. These traits are typical of gabbros emplaced in a post-collisional setting and distinguish them from the early phase of subduction-related gabbroic rocks in the ANS, which are metamorphosed and deformed (e.g. Khalil *et al.* 2015; Surour *et al.* 2017; Gahlan *et al.* 2018).

On the Ca–Ti diagram, clinopyroxene compositions plot in the orogenic/non-orogenic basalts fields (Fig. 4e) (Leterrier *et al.* 1982). The Al^{iv}–Ti diagram shows affinity to island-arc tholeiites (IAT) (Fig. 11a; Beccaluva *et al.* 1989). Moreover, they show a trend transitional between arc- and rift-cumulate rocks (Fig. 11b). These transitional features of clinopyroxenes are possibly due to emplacement in a post-collisional setting during an extensional phase. The Cr-spinels have Cr no. and Mg no. values similar to those of subduction-related rocks in New Georgia (Fig. 11c; Ramsay *et al.* 1984). In addition, their values are comparable to those of layered gabbroic intrusions emplaced during post-collisional extension (Abdel Halim *et al.* 2016). Primary calcic amphiboles and An-rich plagioclases usually crystallized from hydrous magmas with arc-like signatures (Jakes & White, 1972; Hébert & Laurent, 1990; Ballantyne, 1992).

The trace-element and REE patterns of the studied gabbros are comparable to those of gabbros formed in a post-collisional setting (Fig. 7). According to the SiO_2–K_2O correlation and AFM diagram (Fig. 12a, b), they show arc-tholeiitic-like features with a slight calc-alkaline tendency. The Ti–V diagram (Fig. 12c) shows a transitional character between IAT and mid-ocean ridge basalt (MORB). All these implications are in harmony with the pyroxene

https://doi.org/10.1017/S0016756821000182 Published online by Cambridge University Press

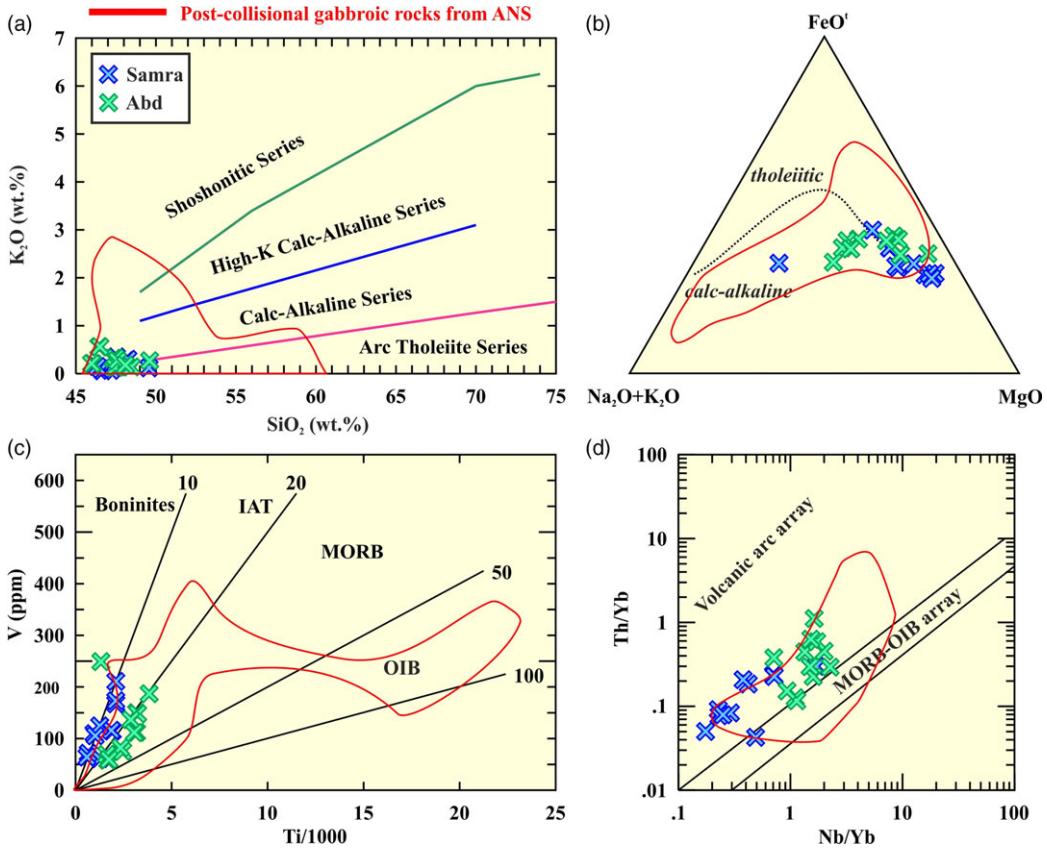

Fig. 12. (Colour online) (a) K_2O–SiO_2 diagram (Peccerillo & Taylor, 1976). (b) AFM diagram. The dashed line separating tholeiitic and calc-alkaline rocks is after Irvine & Baragar (1971). (c) V–Ti diagram (Shervais, 1982). (d) Th/Yb–Nb/Yb diagram (Pearce, 2008). Post-collisional gabbroic rocks from the ANS are shown for comparison (Khalil *et al.* 2015; Surour *et al.* 2017; Eldougdoug *et al.* 2020). Abbreviations: IAT – island-arc tholeiite; MORB – mid-ocean ridge basalt; OIB – ocean-island basalt.

data (Fig. 4d–f). Additionally, the Nb/U ratios are comparable to those of basalts having island-arc-like features (Fig. 10a). On the Th/Yb–Nb/Yb diagram, they plot above the mid-ocean ridge – ocean-island basalt (MORB–OIB) array and within the volcanic arc array, indicating subduction-like characters (Fig. 12d). These geochemical features resemble those of post-collisional gabbroic rocks from the ANS (Fig. 12). It is important to note that the discrimination diagrams cannot distinguish between arc and post-collisional settings. We suggest that the arc- and subduction-like characters displayed by the pyroxene and spinel compositions and by the bulk-rock compositions were likely inherited from the previous subduction event in the ANS.

We conclude that the post-collisional mafic magmatism in the Arabian Shield was probably produced owing to lithospheric extension and upwelling of asthenospheric mantle at the end of the Pan-African orogenic cycle. Moreover, the lithospheric extension is most likely related to the activity of the Najd Fault System. In summary, the geological field relations supported by mineralogical features and geochemical data argue for generation of the studied gabbros during post-collisional extension.

7. Conclusions

The gabbroic rocks of Saudi Arabia represent an important part of the mafic magmatism in the Neoproterozoic Arabian Shield. The present study focused on the gabbroic rocks located in the Gabal Samra and Gabal Abd areas of the Hail region, which belongs to the Arabian Shield of Saudi Arabia. Geological field relations and studies, reinforced by mineralogical and geochemical data, demonstrate their largely unmetamorphosed and undeformed nature, and indicate emplacement in a post-collisional regime. Their mineralogical and geochemical characteristics suggest crystallization from hydrous, mainly tholeiitic, mafic magmas, possibly with inherited arc-like signatures from the previous subduction process in the ANS.

The studied gabbros have Nb/U, Nb/Ta and Zr/Hf ratios below chondritic values, suggesting depletion of their mantle source. Additionally, the elevated $(Gd/Yb)_N$ and $(Dy/Yb)_N$ ratios reflect derivation from a garnet-peridotite source with a garnet signature in the mantle residue. This inference indicates melting at a depth greater than ~70–80 km at the garnet stability field. They have geochemical features comparable to other post-collisional gabbros of the Arabian Shield. The present study suggests that the gabbroic rocks could have originated by adiabatic decompression melting of a depleted asthenospheric mantle, followed by interaction during ascent with metasomatized lithospheric mantle in an extensional regime, likely related to the Najd Fault System activity, at the end of the Pan-African Orogeny.

Acknowledgements. The authors would like to thank Prof. Mohamed Abd El-Wahed, Tanta University, for redrawing the geological maps. We are also grateful to Prof. Shehta E. Abdallah, Zagazig University, for providing mineral and bulk-rock chemistry. The editor Dr Kathryn Goodenough and two anonymous referees are greatly thanked for their valuable suggestions and comments, which indeed helped us to improve the manuscript. This research received no specific grant from any funding agency, commercial or not-for-profit sectors.

Supplementary material. To view supplementary material for this article, please visit https://doi.org/10.1017/S0016756821000182

References

Abdallah SE, Ali S and Obeid MA (2019) Geochemistry of an Alaskan-type mafic-ultramafic complex in Eastern Desert, Egypt: new insights and constraints on the Neoproterozoic island arc magmatism. *Geoscience Frontiers* **10**, 941–55. doi: 10.1016/j.gsf.2018.04.009.

Abdallah SE, Azer MK and Alshammari AS (2020) The petrological and geochemical evolution of Ediacaran rare-metal bearing A-type granites from the Jabal Aja Complex, Northern Arabian Shield, Saudi Arabia. *Acta Geologica Sinica (English Edition)* **94**, 743–62.

Abdel Halim A, Helmy HM, Abdel-Rahman YM, Shibata T, El-Mahallawi MM, Yoshikawa M and Arai S (2016) Petrology of the Motaghairat mafic–ultramafic complex, Eastern Desert, Egypt: a high-Mg post-collisional extension-related layered intrusion. *Journal of Asian Earth Sciences* **116**, 164–80.

Abdel-Karim AM, Ali S and El-Shafei SA (2018) Mineral chemistry and geochemistry of ophiolitic metaultramafics from Um Halham and Fawakhir, Central Eastern Desert, Egypt. *International Journal of Earth Sciences* **107**, 2337–55. doi: 10.1007/s00531-018-1601-2.

Abdel-Karim AM, Ali S, Helmy HM and El-Shafei SA (2016) Fore-arc setting of the Gerf ophiolite, Eastern Desert, Egypt: evidence from mineral chemistry and geochemistry of ultramafites. *Lithos* **263**, 52–65.

Abdel-Karim AM, El-Awady AA, Helmy HM, El-Afandy AH and Abdallah SE (2011) Younger gabbros from Egypt: a transition from tholeiitic to alkaline basaltic magma and from arc to within plate rifting regime. In *The 6th Environmental Conference, 2011, Faculty of Science, Zagazig University, Zagazig, Egypt,* pp. 194–220.

Abd El-Rahman Y, Helmy HM, Shibata T, Yoshikawa M, Arai S and Tamura A (2012) Mineral chemistry of the Neoproterozoic Alaskan-type Akarem Intrusion with special emphasis on amphibole: implications for the pluton origin and evolution of subduction-related magma. *Lithos* **155**, 410–25.

Abdelsalam MG and Stern RJ (1996) Sutures and shear zones in the Arabian–Nubian Shield. *Journal of African Earth Sciences* **23**, 289–310.

Abu-Alam TS, Santosh M, Brown M and Stüwe K (2013) Gondwana collision. *Mineralogy and Petrology* **107**, 631–4.

Agata T and Adachi M (2014) Chrome spinel in normal MORB-type greenstones from the Paleozoic-Mesozoic Mino Terrane, east Takayama area, central Japan: crystallization course with a U-turn. *Island Arc* **23**, 62–73.

Ali KA, Kröner A, Hegner E, Wong J, Li S-Q, Gahlan HA and Abu El Ela FF (2015) U–Pb zircon geochronology and Hf–Nd isotopic systematics of Wadi Beitan granitoid gneisses, South Eastern Desert, Egypt. *Gondwana Research* **27**, 811–24.

Ali S and Ntaflos T (2011) Alkali basalts from Burgenland, Austria: petrological constraints on the origin of the westernmost magmatism in the Carpathian–Pannonian region. *Lithos* **121**, 176–88.

Ali S, Ntaflos T and Sami M (2020) Geochemistry of Khor Um-Safi ophiolitic serpentinites, central Eastern Desert, Egypt: implications for Neoproterozoic arc-basin system in the Arabian-Nubian shield. *Geochemistry*, published online 15 October 2020. doi: 10.1016/j.chemer.2020.125690.

Ali S, Ntaflos T and Upton BGJ (2013) Petrogenesis and mantle source characteristics of Quaternary alkaline mafic lavas in the western Carpathian–Pannonian Region, Styria, Austria. *Chemical Geology* **337–338**, 99–113.

Anderson JL and Smith DR (1995) The effects of temperature and fO_2 on the Al-in-hornblende barometer. *American Mineralogist* **80**, 549–59.

Arndt NT and Christensen U (1992) The role of lithospheric mantle in continental flood volcanism: thermal and geochemical constraints. *Journal of Geophysical Research* **97**, 10967–81.

Azer MK and El-Gharbawi RI (2011) The Neoproterozoic layered mafic-ultramafic intrusion of Gabal Imleih, south Sinai, Egypt: implications of post-collisional magmatism in the north Arabian–Nubian Shield. *Journal of African Earth Sciences* **60**, 253–72.

Azer MK, Obeid MA and Gahlan HA (2016) Late Neoproterozoic layered mafic intrusion of arc-affinity in the Arabian-Nubian Shield: a case study from the Shahira layered mafic intrusion, southern Sinai, Egypt. *Geologica Acta* **14**, 237–59.

Ballantyne P (1992) Petrology and geochemistry of the plutonic rocks of the Halmahera ophiolite, eastern Indonesia, an analogue of modern oceanic forearcs. In *Ophiolites and their Modern Oceanic Analogues* (eds LM Parson, BJ Murton and P Browning), pp. 179–202. Geological Society of London, Special Publication no. 60.

Barrett TJ and MacLean WH (1994) Chemostratigraphy and hydrothermal alteration in exploration for VHMS deposits in greenstone and younger volcanic rocks. In *Alteration and Alteration Processes Associated with Ore-Forming Systems* (ed. DR Lentz), pp. 433–67. Geological Association of Canada, Short Course Notes 11.

Beccaluva L, Macciota G, Piccardo GB and Zeda O (1989) Clinopyroxene composition of ophiolitic basalts as petrogenetic indicator. *Chemical Geology* **77**, 165–82.

Be'eri-Shlevin Y, Katzir Y and Whitehouse M (2009) Post-collisional tectono-magmatic evolution in the northern Arabian–Nubian Shield: time constraints from ion-probe U–Pb dating of zircon. *Journal of the Geological Society, London* **166**, 71–85.

Blundy J, Robinson J and Wood B (1998) Heavy REE are compatible in clinopyroxene on the spinel lherzolite solidus. *Earth and Planetary Science Letters* **160**, 493–504. doi: 10.1016/S0012-821X(98)00106-X.

Bonin B (2004) Do coeval mafic and felsic magmas in post-collisional to within-plate regimes necessarily imply two contrasting, mantle and crustal, sources? A review. *Lithos* **78**, 1–24. doi: 10.1016/j.lithos.2004.04.042.

Carmichael IS, Turner FJ and Verhoogen J (1974) *Igneous Petrology*. New York: McGraw-Hill.

Cisterna CE, Koukharsky M, Coira B, Günter C and Ulbrich HH (2017) Arenigian tholeiitic basalts in the Famatina Ordovician basin, northwestern Argentina: emplacement conditions and their tectonic significance. *Andean Geology* **44**, 123–46. doi: 10.5027/andgeoV44n2-a02.

Collenette P and Grainger DJ (1994) *Mineral Resources of Saudi Arabia*. Directorate General of Mineral Resources Special Publication SP-2. Jeddah: Kingdom of Saudi Arabia Ministry of Petroleum and Mineral Resources.

Condie KC (2003) Incompatible element ratios in oceanic basalts and komatiites: tracking deep mantle sources and continental growth rates with time. *Geochemistry, Geophysics, Geosystems* **4**, 1–28. doi: 10.1029/2002GC000333.

Deer WA, Howie RA and Zussman J (1992) *An Introduction to the Rock-Forming Minerals*. London: Longman Scientific and Technical Publishing.

Defant MJ, Jackson TE and Drummond MS (1992) The geochemistry of young volcanism throughout western Panama and southeastern Costa Rica: an overview. *Journal of the Geological Society, London* **149**, 569–79.

Delfour J (1981) Geologic, tectonic, and metallogenic evolution of the northern part of the Precambrian Arabian Shield (Kingdom of Saudi Arabia). *Bulletin du Bureau de Recherches Géologiques et Minières (deuxieme serie)*, **Section II** (nos. 1–2), 1–19.

Dick HJB and Bullen T (1984) Chromian spinel as a petrogenetic indicator in abyssal and alpine-type peridotites and spatially associated lavas. *Contributions to Mineralogy and Petrology* **86**, 54–76.

Dilek Y and Furnes H (2011) Ophiolite genesis and global tectonics: geochemical and tectonic fingerprinting of ancient oceanic lithosphere. *Geological Society of America Bulletin* **123**, 387–411.

Dixon TH (1981) Gebel Dahanib, Egypt: a late Precambrian layered sill of komatiitic composition. *Contributions to Mineralogy and Petrology* **76**, 42–52.

Ekren EB, Vaslet D, Berthiaux A, Le Strat P and Fourniguet J (1987) Geologic Map of the Ha'il Quadrangle, Sheet 27E, Kingdom of Saudi Arabia, Scale 1:250,000. Jeddah: Deputy Ministry for Mineral Resources, Kingdom of Saudi Arabia Ministry of Petroleum and Mineral Resources.

Eldougdoug A, Abd El-Rahman Y and Harbi H (2020) The Ediacaran post-collisional Khamal gabbro-anorthosite complex from the Arabian Shield and its Fe-Ti-P ore: an analogy to Proterozoic massif-type anorthosites. *Lithos* **372–373**, 105674. doi: 10.1016/j.lithos.2020.105674.

El Gaby S, List FK and Tehrani R (1990) The basement complex of the Eastern Desert and Sinai. In *The Geology of Egypt* (ed. R Said), pp. 175–84. Rotterdam: A. A. Balkema.

El-Mettwaly A (1992) Pan-African post-orogenic gabbro cumulates from Sinai massif, Egypt: geochemistry and mineral chemistry. *Journal of African Earth Sciences* **14**, 217–25.

El Ramly MF (1972) A new geological map for the basement rocks in the Eastern and South-Western Desert of Egypt. *Annals Geological Survey Egypt* **2**, 1–18.

El Sharkawy MA and El Bayoumi RM (1979) The ophiolites of Wadi Ghadir area, Eastern Desert, Egypt. *Annals Geological Survey Egypt* **9**, 125–35.

Eyuboglu Y, Dilek Y, Bozkurt E, Bektas O, Rojay B and Sen C (2010) Structure and geochemistry of an Alaskan-type ultramafic–mafic complex in the Eastern Pontides, NE Turkey. *Gondwana Research* **18**, 230–52.

Eyuboglu Y, Dudás FÖ, Santosh M, Zhu DC, Yi K, Chatterjee N, Jeong YJ, Akaryali E and Liu Z (2016) Cenozoic forearc gabbros from the northern zone of the Eastern Pontides Orogenic Belt, NE Turkey: implications for slab window magmatism and convergent margin tectonics. *Gondwana Research* **33**, 160–89.

Farahat ES and Ali S (2019) Origin and geotectonic evolution of Mir Tertiary basaltic andesite dykes, Western Desert, Egypt: constraints from mineral and bulk-rock chemistry. *Geological Journal* **54**, 2274–87. doi: 10.1002/gj.3296.

Farahat ES, Ali S and Hauzenberger C (2017) Red Sea rift-related Quseir basalts, central Eastern Desert, Egypt: petrogenesis and tectonic processes. *Bulletin of Volcanology* **79**, 9. doi: 10.1007/s00445-016-1092-6

Fleet M and Barnett RL (1978) Al^{iv}/Al^{vi} partitioning in calciferous amphiboles from the mine, Sudbury. Ontario. *Canadian Mineralogist* **16**, 527–32.

Fodor RV and Keil K (1979) Review of the mineral chemistry of volcanic rocks from Maui, Hawaii. In Hawaii Symposium on Intraplate Volcanism and Submarine Volcanism: Abstract Volume, pp. 93–106.

Gahlan HA, Obeid MA, Azer MK and Asimow PD (2018) An example of post-collisional appinitic magmatism with an arc-like signature: the Wadi Nasb mafic intrusion, north Arabian–Nubian Shield, south Sinai, Egypt. *International Geology Review* **60**, 865–88. doi: 10.1080/00206814.2017.1360804.

Giret A, Bonin B and Léger JM (1980) Amphibole compositional trend in oversaturated and undersaturated alkaline plutonic ring complexes. *Canadian Mineralogist* **18**, 481–95.

Gualda GAR and Vlach SRF (2005) Stoichiometry-based estimates of ferric iron in calcic, sodic-calcic and sodic amphiboles: a comparison of various methods. *Anais da Academia Brasileira de Ciências* **77**, 521–34.

Harbi HM (2008) Geology and lithostratigraphy of ultramafic–mafic rocks and associated mineralization Wadi Khamal area, Western Saudi Arabia. *King Abdulaziz University Journal of Earth Sciences* **19**, 119–57.

Hawkesworth CJ, Gallagher K, Hergt JM and McDermott F (1993) Mantle and slab contributions in arc magmas. *Annual Review of Earth and Planetary Sciences* **21**, 175–204.

Hébert R and Laurent R (1990) Mineral chemistry of the plutonic section of the Troodos ophiolite: new constraints for genesis of arc-related ophiolites. In *Ophiolites, Oceanic Crustal Analogues: Proceedings of the Symposium "Troodos 1987"* (eds J Malpas, EM Moores, A Panayiotou and C Xenophontos), pp. 149–63. Nicosia: Geological Survey Department.

Helmy HM, Yoshikawa M, Shibata T, Arai S and Kagami H (2015) Sm–Nd dating and petrology of Abu Hamamid intrusion, Eastern Desert, Egypt: a case of Neoproterozoic Alaskan-type complex in a back-arc setting. *Precambrian Research* **258**, 234–46.

Hofmann AW (1997) Mantle geochemistry: the message from oceanic volcanism. *Nature* **385**, 219–29.

Hofmann AW, Jochum KP, Seufert M and White WM (1986) Nb and Pb in oceanic basalts, new constraints on mantle evolution. *Earth and Planetary Science Letters* **79**, 33–45.

Irvine TN (1965) Chromian spinel as a petrogenetic indicator: Part I. Theory. *Canadian Journal of Earth Sciences* **2**, 648–72.

Irvine TN and Baragar WRA (1971) A guide to the chemical classification of the common volcanic rocks. *Canadian Journal of Earth Sciences* **8**, 523–48.

Jakes P and White A (1972) Hornblendes from calc-alkaline volcanic rocks of island arcs and continental margins. *American Mineralogist* **57**, 887–902.

Jochum KP, Seufert HM, Spettel B and Palme H (1986) The solar-system abundances of Nb, Ta, and Y, and the relative abundances of refractory lithophile elements in differentiated planetary bodies. *Geochimica et Cosmochimica Acta* **50**, 1173–83.

Johnson PR, Andresen A, Collins AS, Fowler AR, Fritz H, Ghebreab W, Kusky T and Stern RJ (2011) Late Cryogenian–Ediacaran history of the Arabian-Nubian Shield: a review of depositional, plutonic, structural, and tectonic events in the closing stages of the northern East African Orogen. *Journal of African Earth Sciences* **61**, 167–232.

Johnson PR, Halverson GP, Kusky T, Stern RJ and Pease V (2013) Volcanosedimentary basins in the Arabian–Nubian Shield: markers of repeated exhumation and denudation in a Neoproterozoic accretionary orogen. *Geosciences* **3**, 389–445.

Johnson PR and Woldehaimanot B (2003) Development of the Arabian–Nubian Shield: perspectives on accretion and deformation in the northern East African Orogen and assembly of Gondwana. In *Proterozoic East Gondwana: Supercontinent Assembly and Breakup* (eds M Yoshida, BF Windley and S Dasgupta), pp. 289–326. Geological Society of London, Special Publication no. 206.

Kakar MI, Kerr AC, Mahmood K, Collins AS, Khan M and McDonald I (2014) Supra-subduction zone tectonic setting of the Muslim Bagh Ophiolite, northwestern Pakistan: insights from geochemistry and petrology. *Lithos* **202–203**, 190–206.

Kellogg KS (1983) *Reconnaissance Geology of the Qufar Quadrangle, Sheet 27/41 D, Kingdom of Saudi Arabia*. Kingdom of Saudi Arabia Deputy Ministry for Mineral Resources. United States Geological Survey Open-File Report 84-159, 35 pp.

Kellogg KS and Stoeser DB (1985) *Reconnaissance Geology of the Hail Quadrangle, Kingdom of Saudi Arabia*. Kingdom of Saudi Arabia Deputy Ministry for Mineral Resources. United States Geological Survey Open-File Report 85-618, 35 pp.

Khalil AES, Obeid MA and Azer MK (2015) Late Neoproterozoic post-collisional mafic magmatism in the Arabian–Nubian Shield: a case study from Wadi El-Mahash gabbroic intrusion in southeast Sinai, Egypt. *Journal of African Earth Sciences* **105**, 29–46.

Kodolanyi J, Pettke T, Spandler C, Kamber BS and Gmeling K (2012) Geochemistry of ocean floor and fore-arc serpentinites: constraints on the ultramafic input to subduction zones. *Journal of Petrology* **53**, 235–70.

Koepke J, Feig ST, Snow J and Freise M (2004) Petrogenesis of oceanic plagiogranites by partial melting of gabbros: an experimental study. *Contributions to Mineralogy and Petrology* **146**, 414–32.

Kröner A and Stern RJ (2004) Africa: Pan-African orogeny. In *Encyclopedia of Geology* (eds R Shelley, LRM Cocks and IR Pilmer), pp. 1–12. Amsterdam: Elsevier.

Kun L, Ruidong Y, Wenyong C, Rui L and Ping T (2014) Trace element and REE geochemistry of the Zhewang gold deposit, southeastern Guizhou Province, China. *Chinese Journal of Geochemistry* **33**, 109–18.

Kushiro I (1990) Partial melting of mantle wedge and evolution of island arc crust. *Journal of Geophysical Research: Solid Earth* **95**, 15929–39.

Kushiro I and Mysen BO (2002) A possible effect of melt structure on the Mg-Fe^{2+} partitioning between olivine and melt. *Geochimica et Cosmochimica Acta* **66**, 2267–72.

Leake BE, Woolley AR, Birch WD, Burke EAJ, Ferraris G, Grice JD, Hawthorne FC, Kisch HJ, Krivovichev VG, Schumacher JC, Stephenson NCN and Whittaker EJW (2004) Nomenclature of amphiboles: additions and revisions to the International Mineralogical Association's amphibole nomenclature. *European Journal of Mineralogy* **16**, 191–6.

Le Bas MJ (1962) The role of aluminum in igneous clinopyroxenes with relation to their parentage. *American Journal of Science* **260**, 267–88.

Leterrier J, Maury RC, Thonon P, Girard D and Marchal M (1982) Clinopyroxene composition as a method of identification of the magmatic affinities of paleo-volcanic series. *Earth and Planetary Science Letters* **59**, 139–54.

Loucks RR (1990) Discrimination of ophiolitic from nonophiolitic ultramafic–mafic allochthons in orogenic belts by the Al/Ti ration in clinopyroxene. *Geology* **18**, 346–9.

Martel C, Pichavant M, Bourdier J-L, Traineau H, Holtz F and Scaillet B (1998) Magma storage conditions and control of eruption regime in silicic volcanoes: experimental evidence from Mt. Pelée. *Earth and Planetary Science Letters* **156**, 89–99.

Meert JG (2003) A synopsis of events related to the assembly of eastern Gondwana. *Tectonophysics* **362**, 1–40.

Middlemost EAK (1994) Naming materials in the magma/igneous rock system. *Earth-Science Reviews* **37**, 215–24.

Mogahed MM (2019) Petrogenesis of Zeiatit gabbroic rocks in the Southern Eastern Desert of Egypt: discrimination of arc-related Neoproterozoic

https://doi.org/10.1017/S0016756821000182 Published online by Cambridge University Press

gabbros. *Journal of African Earth Sciences* **150**, 239–63. doi: 10.1016/j.jafrearsci.2018.11.007.

Morimoto N, Fabries J, Ferguson AK, Ginzburg IV, Ross M, Seifert FA, Zussman J, Aoki K and Gottardi G (1988) Nomenclature of pyroxenes. *Mineralogical Magazine* **52**, 535–50.

Mysen B (2014) Water-melt interaction in hydrous magmatic systems at high temperature and pressure. *Progress in Earth and Planetary Science* **1**, 4. doi: 10.1186/2197-4284-1-4.

Nachit H, Ibhi A, Abia EA and Ohoud MB (2005) Discrimination between primary magmatic biotites, re-equilibrated biotites and neo-formed biotites: *Comptes Rendus Geoscience* **337**, 1415–20. doi: 10.1016/j.crte.2005.09.002.

Panjasawatwong Y, Danyushevsky LV, Crawford AJ and Harris KL (1995) An experimental study of the effects of melt composition on plagioclase-melt equilibria at 5 and 10 kbar: implications for the origin of magmatic high-An plagioclase. *Contributions to Mineralogy and Petrology* **118**, 420–32.

Pearce JA (1996) A user's guide to basalt discrimination diagrams. In *Trace Element Geochemistry of Volcanic Rocks: Applications for Massive Sulphide Exploration* (ed. DA Wyman), pp. 79–113. Geological Association of Canada, Short Course Notes 12.

Pearce JA (2008) Geochemical fingerprinting of oceanic basalts with applications to ophiolite classification and the search for Archean oceanic crust. *Lithos* **100**, 14–48.

Peccerillo A and Taylor SR (1976) Geochemistry of Eocene calc-alkaline volcanic rocks from the Kastamonu area, Northern Turkey. *Contributions to Mineralogy and Petrology* **58**, 63–81.

Plank T (2005) Constraints from thorium/lanthanum on sediment recycling at subduction zones and the evolution of the continents. *Journal of Petrology* **46**, 921–44.

Polat A and Hofmann AW (2003) Alteration and geochemical patterns in the 3.7–3.8 Ga Isua greenstone belt, West Greenland. *Precambrian Research* **126**, 197–218.

Prouteau G, Scaillet B, Pichavant M and Maury R (2001) Evidence for mantle metasomatism by hydrous silicic melts derived from subducted oceanic crust. *Nature* **410**, 197–200.

Ramsay WHR, Crawford AJ and Foden JD (1984) Field setting, mineralogy, chemistry, and genesis of arc picrites, New Georgia, Solomon Islands. *Contributions to Mineralogy and Petrology* **88**, 386–402.

Robinson F, Foden J and Collins A (2015a) Geochemical and isotopic constraints on island arc, synorogenic, post-orogenic and anorogenic granitoids in the Arabian Shield, Saudi Arabia. *Lithos* **220–223**, 97–115. doi: 10.1016/j.lithos.2015.01.021.

Robinson F, Foden JD and Collins A (2015b) Zircon geochemical and geochronological constraints on contaminated and enriched mantle sources beneath the Arabian Shield, Saudi Arabia. *The Journal of Geology* **123**, 463–89. doi: 10.1086/683192.

Rudnick RL and Gao S (2003) The composition of the continental crust. In *Treatise on Geochemistry, Volume 3: The Crust* (eds RL Rudnick, HD Holland and KK Turekian), pp. 1–64. Oxford: Elsevier.

Sack RO and Ghiorso MS (1991) Chromite as a petrogenetic indicator. *Reviews in Mineralogy and Geochemistry* **25**, 323–53.

Saunders AD, Storey M, Kent RW and Norry MJ (1992) Consequences of plume-lithosphere interactions. In *Magmatism and the Cause of Continental Breakup* (eds BC Storey, T Alabaster and RJ Pankhurst), pp. 41–60. Geological Society of London, Special Publication no. 68.

Schiano P, Clocchiatti R, Shimuzu N, Maury RC, Jochum KP and Hofmann AW (1995) Hydrous silica-rich melts in the sub-arc mantle and their relationship with erupted arc lavas. *Nature* **377**, 595–600.

Schmidt MW (1992) Amphibole composition in tonalite as a function of pressure: an experimental calibration of the Al-in-hornblende barometer. *Contributions to Mineralogy and Petrology* **110**, 304–10.

Sedki T, Ali S and Mohamed HA (2019) Geochemical characterization of the Sol Hamed Neoproterozoic ophiolitic serpentinites, Southern Eastern Desert, Egypt. In *7th International Large Igneous Provinces (LIP) Conference, Tomsk State University, Tomsk, Russia, 28 August – 8 September 2019, Abstract Volume*, pp. 136–7.

Shervais JW (1982) Ti–V plots and the petrogenesis of modern ophiolitic lavas. *Earth and Planetary Science Letters* **59**, 101–18.

Sigurdsson H and Schilling JG (1976) Spinels in Mid-Atlantic Ridge basalts: chemistry and occurrence. *Earth and Planetary Science Letters* **29**, 7–20.

Sisson T and Grove T (1993) Experimental investigations of the role of H_2O in calc-alkaline differentiation and subduction zone magmatism. *Contributions to Mineralogy and Petrology* **113**, 143–66.

Stern RJ (2002) Crustal evolution in the East African Orogen: a neodymium isotopic perspective. *Journal of African Earth Sciences* **34**, 109–17.

Stoeser DB and Frost CD (2006) Nd, Pb, Sr, and O isotopic characterization of Saudi Arabian Shield terranes. *Chemical Geology* **226**, 163–88.

Sun S-S and McDonough WF (1989) Chemical and systematic of ocean basalts: implications for mantle composition and processes. In *Magmatism in Ocean Basins* (eds AD Saunders and MJ Norry), pp. 313–45. Geological Society of London, Special Publication no. 42.

Surour AA, Ahmed AH and Harbi HM (2017) Mineral chemistry as a tool for understanding the petrogenesis of Cryogenian (arc-related) – Ediacaran (post-collisional) gabbros in the western Arabian Shield of Saudi Arabia. *International Journal of Earth Sciences* **106**, 1597–617. doi: 10.1007/s00531-016-1371-7

Takla MA, Basta EZ and Fawzi E (1981) Characterization of the older and younger gabbros of Egypt. *Delta Journal Science* **5**, 279–314.

Tang Y-J, Zhang H-F and Ying J-F (2006) Asthenosphere–lithospheric mantle interaction in an extensional regime: implication from the geochemistry of Cenozoic basalts from Taihang Mountains, North China Craton. *Chemical Geology*, **233**, 309–27.

Taylor SR and McLennan SM (1995) *The Continental Crust: Its Composition and Evolution*. Oxford: Blackwell, 312 pp.

Wager LR and Brown GM (1967) *Layered Igneous Rocks*. Edinburgh: Oliver and Royd, 588 pp.

Wallace PJ (2005) Volatiles in subduction zone magmas: concentrations and fluxes based on melt inclusion and volcanic gas data. *Journal of Volcanology and Geothermal Research* **140**, 217–40.

Walter MJ (1998) Melting of garnet peridotite and the origin of komatiite and depleted lithosphere. *Journal of Petrology* **39**, 29–60.

Wicks FJ and Plant AG (1979) Electron microprobe and X-ray microbeam studies of serpentine textures. *Canadian Mineralogist* **17**, 785–830.

Yang S-H and Zhou M-F (2009) Geochemistry of the ~430-Ma Jingbulake mafic–ultramafic intrusion in Western Xinjiang, NM China: implications for subduction related magmatism in the South Tianshan orogenic belt. *Lithos* **113**, 259–73.

https://doi.org/10.1017/S0016756821000182 Published online by Cambridge University Press